Master Thesis

Synthesis and Characterization of the solid solution series $ZnFe_2O_4$-$ZnAl_2O_4$

From

Meriem Machitouen

Master of Science | Chemical Engineering
Department of Chemical Engineering
FH Münster University of Applied Sciences
Technology Campus Steinfurt

University supervisor
Prof. Dr. rer. nat. Thomas Jüstel

Company supervisor
Dr. Kerstin Neuhaus

Statutory declaration

I declare that I have written the work I have submitted independently. All passages that are taken verbatim or in essence from published or unpublished works by others have been marked as such. All sources that I have used for the work have been indicated.

Meriem Machitouen
April 1st, 2025
Steinfurt, Germany

This work has been conducted in the time frame from October 1st, 2024 to March 31st, 2025 at the Institute of energy materials and devices (IMD-4): Helmholtz-Institute Münster: Ionics in energy storage (HIMS).

Company supervisor: Dr. Kerstin Neuhaus

Address:

Forschungszentrum Jülich GmbH
Institute of Energy Materials and Devices (IMD-4)
Helmholtz-Institut Münster: Ionenleiter für Energiespeicher (HIMS)
Corrensstr. 48
D-48341 Münster
Deutschland

FH supervisor: Prof. Dr. rer. nat. Thomas Jüstel

Address:

Fachhochschule Münster
Fachbereich Chemieingenieurwesen
Stegerwaldstraße 39
D-48565 Steinfurt
Deutschland

This thesis was submitted to the examination board of the Department of Chemical Engineering on April 1st, 2025.

Acknowledgements and thanks

First and foremost, I would like to express my sincere thanks to Dr. Kerstin Neuhaus for the opportunity to join her team and for the chance to work on this fascinating topic. Furthermore, I would like to express my deep gratitude for her unwavering support and generous sharing of knowledge, as well as for her constant availability and willingness to assist me with any challenges I faced during my work. I am also truly appreciative of her kindness and her ability to ease my stress—she always knew how to create a calm and relaxed atmosphere, making the work environment incredibly pleasant and enjoyable.

My thanks also go to Patrick Mowe, who has been an incredible support throughout this process. He was always ready to help with any issues I encountered, and consistently made an effort to ease any concerns or challenges I had. His kindness, willingness to assist with everything, and constant availability made a significant difference, and I truly appreciate his approachability and generosity in offering his help whenever needed.

Furthermore, I would like to thank Susanna Krämer for her invaluable assistance with cathode preparation and cell construction. She was not only kind and patient but also generously gave her time to help whenever I needed her expertise. I truly appreciate her support and willingness to assist whenever I needed guidance.

I would also like to express my thanks to Professor Thomas Jüstel as well for his supervision and continuous support throughout this project. His dedication and active involvement were greatly appreciated, and I am thankful for his willingness to answer my questions and provide valuable guidance via email.

Last but not least, I would like to express my heartfelt thanks to my family for their unwavering support and encouragement throughout my entire higher education journey.

Table of Contents

1. Introduction

As the use of fossil fuels increases, so does the CO_2 in the atmosphere, which has driven global warming. This triggers an urgent need to reconsider how one uses energy in everyday life. If new energy storage technologies are to emerge, they must be based on safe, cheap and sustainable systems.

As a solution to achieve this goal, Li-ion batteries (LIBs) have revolutionized communication and transportation industries with high energy density, prolonged cycle life and lightweight design.[1] Because of this many electric vehicles (EVs) are now powered by LIBs, however when it comes to large-scale applications, the availability of lithium and safety concerns related to LIB become a problem. There have been reports about several accidents involving the explosion and ignition of LIBs, because of the employment of very flammable and organic electrolytes. There has been research involving rechargeable aqueous LIBs. However, one of the faced challenges in the application of aqueous electrolyte with lithium-ion batteries is the extremely lowered electrochemical stability window compared to organic electrolyte, as well as the parasitic reactions. [2]

Also, it should be noted that it is estimated that making 1 kWh LIB results in an emission of almost 75 kg CO_2, and in comparison, generating 1 kWh electricity from coal produces 1 kg CO_2, this means that the environmental benefits of using LIB will only start at beyond hundreds of cycles. [3]

With the rise of renewable energy sources, the demand for stationary storage systems is increasing as well. Although there are existing energy storage devices (ESDs) in stationary applications, there is a motivation for use of next generation ESDs like future Li-ion, solid state, metal ion batteries and others. However, there is a gap that requires further study and verification for these applications.[4]

Some plausible alternatives to LIBs are Na-ion and K-ion batteries since they are based on very abundant and cheap materials. However, they do suffer from low energy density, highly toxic and flammable electrolytes and have high operating costs and safety issues. Rechargeable multivalent metal ion (Mg^{2+}, Ca^{2+}, Zn^{2+}, Al^{3+}) batteries seem promising due to the use of very earth-abundant polyvalent cations and their improved safety and high volumetric energy density.[3], [5]

Zinc is considered a promising element for metal electrode batteries. Zinc as a negative electrode also has a long history, from the voltaic pile, and alkaline batteries to Zn-air batteries.[2]

The reason for using zinc in batteries for more than 200 years is due to electrochemical reversibility, stability in aqueous electrolytes, good electronic conductivity, high abundance, low cost, and low toxicity. Therefore, rechargeable zinc batteries can excel as an alternative for environmentally friendly and safe storage systems.[6] Zinc batteries are most promising in aqueous electrolytes, they are also preferable due to their environmental friendliness, high operational safety, and low cost. Additionally, aqueous electrolytes offer excellent ionic conductivity.[7] It is also a great advantage that zinc metal can be used directly as the anode material, so technically speaking almost all zinc-ion batteries are zinc-metal batteries (ZMBs), even if this has not been consistently accepted in the literature.

In contrast to the well-established energy storage systems, the operational mechanisms in aqueous zinc-ion batteries (AZIBs) are different and are reported to involve generally three processes.[5] Gaining a comprehensive understanding of these mechanisms is essential for enhancing the efficiency and longevity of ZIB systems.

- Zn^{2+} insertion/extraction mechanism: The positive electrode is usually made of materials that are capable of hosting zinc ions, while in most cases metallic zinc serves as a negative electrode. During charging the Zn is oxidized at the negative electrode and releases electrons, which migrate through the electrolyte and are inserted into the positive electrode's structure. During discharge, this process is reversed which means the Zn^{2+} is extracted from the positive electrode and then is reduced to metallic zinc at the negative electrode.[8]

The general mechanism can be explained as follows:

Negative electrode:

$$\mathbf{Zn \leftrightarrow Zn^{2+} + 2e^-} \qquad \text{Eq. 1}$$

Positive electrode:

$$\mathbf{Zn^{2+} + 2e^- + cathode\ material \leftrightarrow intercalated\ cathode\ material} \qquad \text{Eq. 2}$$

- Chemical conversion mechanism: This mechanism involves the transformation of the cathode structure and the formation of a new phase throughout the charge and discharge processes. For example, in ß-MnO_2 during discharge, Zn^{2+} with the involvement of protons results in the formation of zinc hydroxy salts. The MnO_2 structure undergoes a transformation, converting into MnOOH. The mechanism for this material is as follows[9]:

Negative electrode:

$$\mathbf{Zn \leftrightarrow Zn^{2+} + 2e^-} \qquad \text{Eq. 3}$$

Positive electrode:

$$\mathbf{MnO_2 + e^- + H^+ \leftrightarrow MnOOH} \qquad \text{Eq. 4}$$

$$\mathbf{Zn^{2+} + 6OH^- + ZnSO_4 + xH_2O \leftrightarrow ZnSO_4[Zn(OH)_2]_3xH_2O} \qquad \text{Eq. 5}$$

- Deposition/dissolution mechanism: In this mechanism, energy is stored and released through the reversible deposition and dissolution of zinc metal. During the charging process, the zinc ions are reduced and deposited as zinc metal on the negative electrode, during discharge, zinc is oxidized into Zn^{2+} and released into the electrolyte.[10]

There are other proposed mechanisms involved in ZIBs/ZMBs, but unfortunately there is no direct characterization method to reveal the accurate mechanism involved in Zn^{2+} storage.[11]

ZIBs/ZMBs face several challenges that hinder their practical application. Maintaining the structural stability of cathode materials during cycling is problematic. For this reason, most of the research focuses on the exploration and development of cathode materials. At the moment, some of the main materials encompass manganese-based oxides, vanadium-based oxides, Prussian blue analogues, and olivine-based phosphates.

Manganese-based oxides are desirable candidates due to their abundance, eco-friendliness as well as affordability. The charge storage mechanism in Zn||MnO_2 cells relies on the chemical conversion mechanism explained above, which means that the structure goes through multiple structural changes during cycling. The stress induced by such a mechanism promotes electrode detachment from the current collector and decreases the electrochemical performance.[12]

In contrast, vanadium-based intercalation materials also exhibit good performance, [12] their chemical stability and capacity are higher than those of the Mn-based cathodes. However, they display a lower voltage (0.75 V) compared to the Mn-based system (1.3 V).[13]

On the other hand, Prussian blue analogues possess many interstitial sites and tunnels in their crystal structure. This allows easy and reversible insertion/desertion of different ions including Zn^{2+}.[11] However, they face some challenges in their applications such as low electronic conductivity, low chemical stability and active material dissolution over cycling[10], as well as the development of highly toxic species during degradation.

The goal of this work is to develop a positive electrode for ZIBs and ZMBs. The material should display the highest possible electron and ion conductivity, and the highest possible voltage, and be cycled without displaying major losses.

Zinc ferrite or $ZnFe_2O_4$ displays good performance in many fields, such as gas sensors, photo-catalysis, solar cells as well as in lithium-ion batteries. The electrical conductivity falls between 5 to 10 $mS \cdot cm^{-1}$, the electronic band gap of 1.9 eV, 2.02 eV, and 2.33 eV for direct and indirect optical bandgap.[14] This material has already been applied as an active material in ZIBs. In previous work, part of the Fe^{3+} was doped with Ti^{4+} to achieve stabilization of Zn vacancies and increase the ionic conductivity. However, the solubility was limited to $x = 0.11$ and the samples with higher amounts of Ti^{4+} did not show a stable cycling behavior. A particular issue with this active material is iron leaching in contact with slightly acidic aqueous electrolyte.[15]

In this work, iron will be replaced with Al^{3+}, $ZnFe_{2-x}Al_xO_4$, at concentrations from $x = 0.0$ to $x = 2.0$. Since Al^{3+} is generally considered non-redox-active (reduction potential at - 1.66 V [16]) in aqueous solutions, it is expected that the structure will be more stable. However, the electronic conductivity is expected to decrease, while the band gap increases— both undesirable for an active material. Additionally, as the aluminum content increases, the material's magnetic susceptibility is expected to decline, and its optical properties are likely to change.

Therefore, the effect of aluminum addition on electrochemical, magnetic and optical parameters are investigated in this work.

2. Theory

2.1. Spinels

The term spinel refers to a diverse class of compounds characterized by the general formula AB_2X_4, the name is derived from the mineral spinel ($MgAl_2O_4$) due to their similar crystal structure. These compounds are predominantly found as oxides, where A and B are metals typically in oxidation states II and III, although combinations of IV and II also exist. The anion X can be O^{2-}, S^{2-}, Se^{2-}, or Te^{2-}. Spinels feature a face-centered cubic (fcc) lattice of X^{2-} anions, stabilized by interstitial cations. [17]

A specific group of spinels that stand out are ferrites, they are magneto-ceramic materials primarily composed of ferric oxide (Fe_2O_4) combined with metal oxides such as MO (M = Mg, Mn, Fe, Zn).[18] A more specific formula for spinel ferrites is $MeFe_2O_4$, where Me represents a divalent metal cation with an ionic radius of approximately 0.6 to 1 Å (e.g., Zn, Mn, Fe, Co, Ni, Mg). This allows for a variety of ferrite solid solutions or mixed ferrites, extending the formula to $MeFe_2\text{-}x^{3+}Me'_xO_4$. [19]

In the cubic structure, O^{2-} ions occupy the ccp lattice sites, while Me and Fe occupy octahedral and tetrahedral positions. A cubic unit cell contains eight fcc cells, comprising 32 O^{2-} anions, 16 cations in octahedral sites, and eight cations in tetrahedral sites.[18] Spinel ferrites can be categorized into two groups based on the arrangement of divalent metal ions and trivalent ferric ions:

1) In normal spinels, tetrahedral sites are occupied by Me and octahedral sites by Fe.
2) In inverse spinels, tetrahedral sites are occupied by Fe, and octahedral sites by Me.

Examples of normal spinel ferrites include zinc ferrite ($ZnFe_2O_4$), and $CdFe_2O_4$, while inverse spinel ferrites include Fe_3O_4 and Ni-Zn ferrites. There is no way to determine from the composition whether a spinel is normal or inverse. Theoretical studies suggest that there is a small energy difference between the two forms and that their relative stabilities are determined by a balance between several factors. [20]

In this study, zinc ferrite ($ZnFe_2O_4$) has been doped with aluminum (Al^{3+}) across a range of concentrations ($ZnFe_{2-x}Al_xO_4$ with x = 0.0 to 2.0), resulting in a solid solution series that is to be investigated and characterized.

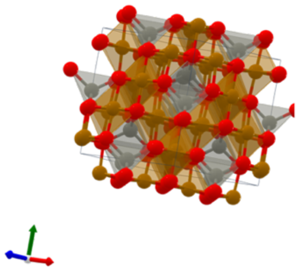

Figure 1 unit cell of $ZnFe_2O_4$, (Zn^{2+} in gray, Fe^{3+} in brown, O^{2-} in red)

The final composition in the series is zinc aluminate, which also belongs to the same crystal structure group. It has a normal spinel structure with all zinc cations occupying the tetrahedral sites and the aluminum cations in the octahedral sites in a cubic structure.[21] Since both zinc ferrite and zinc aluminate crystallize in a cubic spinel structure, it is anticipated that the substitution of Fe^{3+} ions by Al^{3+} ions will lead to a single-phase solid solution. This substitution is expected to influence various properties of the material, including its structural, magnetic, electrical, and optical characteristics.

2.2. Conductivity

- Electronic conductivity

Unlike metals, which have partially or full overlapping valence and conduction bands, semiconductors feature a distinct conduction band. The valence band, located below the band gap, is occupied by electrons, while the conduction band, positioned above the band gap, remains empty. Conduction in semiconductors occurs when electrons gain enough energy to cross the band gap, which can be enhanced by increasing the temperature, photon absorption or introducing substitutional impurities a process also known as doping. [22]

However, the conventional band gap theory fails to capture the behavior of transition metal oxides, this is mainly because the outermost orbitals do not overlap very well with electrons on neighboring atoms. In transition metal oxides this can result in two cases: if these orbitals overlap strongly, as in TiO and VO, electrons can move freely from one atom to another, leading to metallic conductivity. However, in oxides like MnO-, or FeO, weak orbital overlap keeps the electrons localized or trapped on individual atoms, resulting in semiconducting behavior.[22]

When an electron is trapped in an atomic position, its charge distorts the electronic distribution surrounding it. However, the distortion of the lattice around the electron makes it possible to stabilize the system. This quasi-particle is formed by the electron and the polarization surrounding it forms the small polaron and makes electron movement into the conduction band more difficult.[23] As a result, electrons require significantly more energy to transition into the conduction bands, leading to reduced electrical conductivity at lower temperatures. [22] Since charge transport across the conduction band is more challenging for these materials, charge transfer through hopping occurs. Small polaron hopping conduction is a mechanism where electrons jump from one localized site to another. The higher the temperature the better the conductivity for these types of materials. This type of conduction happens in compounds with mixed valence elements. For example, in magnetite (Fe_3O_4), the electrons move between Fe^{2+} and Fe^{3+}.[23] The same mechanism occurs in zinc ferrite. The conduction mechanism is ruled by small polaron hopping.

- Ionic conductivity

In ionic solids, the ions stay fixed at their lattice positions, and do not have enough energy to move away from these sites, however when ions gain enough energy to move from these sites to neighboring unoccupied sites, this movement leads to ionic conduction.[22], [24] Ionic conductivity is dependent on concentration of charge carries, their charge as well as the mobility of those charge carriers. Ionic movement specifically is governed by the diffusion - which relates transport of particle to a concentration gradient- and migration which describes the movement of the charged particles in an electric field. The most general diffusion mechanism is the vacancy meditated diffusion. Some other types for diffusion mechanisms are direct interstitial where the ion jumps from a lattice site to an unoccupied neighbouring interstitial site or the interstitialcy mechanism, in which an ion jumps from a lattice site into an interstitial site that was previously occupied, pushing the interstitial ion into a neighbouring vacant lattice site.[25] For this to happen, there must be adjacent vacant sites that serve as potential jumping points for the ions. These vacant sites which are termed defects must be present in the lattice. A finite concentration of defects is found in all materials at temperatures above 0 K. This means that there is a very small defect concentration in any crystal at each temperature.[26]

There are multiple defects to consider in solids, but those relevant to conductivity can be categorized into two groups: point defects and planar defects

- Point defects are normally also divided into two subgroups:

Intrinsic point defects are physical defects that do not involve any dopants or impurities. These involve lattice vacancies. They include Schottky defects which appear when an atomic site in an ideal structure is not occupied. These types of defects contribute to the diffusion mechanism of ionic charge carriers. On the other hand, interstitial defects or Frenkel defects, involve atoms that have moved from their atomic site to an interstitial site that is normally unoccupied. These defects influence diffusion within materials, they may block the diffusion pathway of mobile ions or if the interstitial sites correspond to the mobile ions, they may increase conductivity.[27], [28]

Extrinsic point defects are chemical defects that do involve modification of the chemical composition of the compound. They involve the substitution of atoms of the original lattice and introducing an extra atom in an empty interstitial site.[27], [28]

- Planar defects are two dimensional defects. They include free surfaces between gas or liquid and the crystal. Grain boundaries where two crystals form the same material meet. Two phase interfaces between two phases of different compositions in the solid. These defects affect the performance of battery materials, by impacting their structure, stability and conductivity. [28]

In most solids, the ionic conductivity is too small to measure at room temperature. However, at higher temperatures, concentration of Schottky and Frenkel defects become more prominent due increasing the number of mobile ions.[29]

- Total conductivity

Understanding the different conduction mechanisms is important for analyzing the conductivity of the material. The total conductivity encompasses the sum of all the partial conductivities of all charge carriers. These charge carriers are cations or anions and electrons, and each might have different contributions from different transport mechanisms.[26]

$$\boldsymbol{\sigma} = \boldsymbol{\sigma}_{\text{ion}} + \boldsymbol{\sigma}_{\text{e}} = \boldsymbol{\sigma}_{\text{cation}} + \boldsymbol{\sigma}_{\text{anion}} + \boldsymbol{\sigma}_{\text{e}} \qquad \text{Eq. 6}$$

σ: total conductivity
σ_{ion}: ionic conductivity
σ_e: electron conductivity
σ_{cation}: cation conductivity
σ_{anion}: anion conductivity

2.3. Synthesis

Sol-gel process is a method to synthesize inorganic polymers or ceramics from solution through the transformation from a liquid precursor to sol which can be defined as a colloidal suspension and then transformed into a network structure called gel.[30]

The Pechini method is a sol-gel synthesis route, the first step of this synthesis is the formation of a stable chelate complex of cations and hydrocarboxylic acid. The cation precursor should be soluble in water or in an aqueous solution with the chelating agent. Nitrates and citric acid are the most frequently utilized substances.

The complex needs to be stable to prevent any inhomogeneity in the final product. The second step is the cross-linking of the chelates through the addition of polyalcohols to create a gel through esterification. The solution is then dried at higher temperatures to remove water, consequently, the viscosity increases, and the solution is turned into a resin-like material. Finally, upon further heating the material turns into a brittle porous material.

The third step in this synthesis is the thermal decomposition to remove the organic part of the resin.[31], [32]

2.4. Sintering

After obtaining the product in powder form, the powder is pressed into the desired shape, this is done to accomplish high packing of ceramic particles and proper connection of the particles to each other. When the sintering temperature reaches 2/3 of the melting point of the product, the particles are intensely bonded together, this increase in the contact area between the grains increases the density of the sintered bodies and decreases porosity. The removal of pores avoids possible microstructure defects, which would alter the characteristics of the resulting product.
The final properties of the ceramic are affected by the process settings. Temperature is a significant parameter for controlling the rate of the changes during sintering, time is also an important factor for improving densification and finally the atmosphere is also crucial for obtaining desirable results. [18]

2.5. Magnetism

Materials can be divided into either magnetic or non-magnetic materials. Magnetic materials show an attraction force of attraction or repulsion to others, for example, iron, cobalt, nickel. Non-magnetic materials, do not produce any force of attraction or repulsion, like plastic, gold, silver…

In the presence of a magnetic field (*H*), this magnetization (*M*) is described as magnetic susceptibility (χ). The relation between all these terms is the following:

$$\chi = \frac{\boldsymbol{M}}{\boldsymbol{H}} \qquad \text{Eq. 7}$$

It can be expressed either as volume susceptibility (χ_v) or mass susceptibility (χ_g).
Through application of a magnetic field (*H*), all materials can be classified as:

- Diamagnetic materials: show negative magnetic susceptibility.
- Paramagnetic materials: show very low but positive magnetic susceptibility.
- Ferromagnetic materials: show high positive magnetic susceptibility.
- Antiferromagnetic materials: show medium positive magnetic susceptibility.[18], [22]

The atomic arrangement in spinel ferrites effect their magnetism, they can either display ferromagnetic or antiferromagnetic behavior, this is due to the magnetic spins in the octahedral and tetrahedral sites. For example, in zinc ferrite, zinc does not contribute to the magnetism, if however, Fe^{3+} is found in equal numbers in both octahedral and tetrahedral sites (in case of some degree of inversion), this means that there are equal numbers of Fe^{3+} spins pointing in two different direction and thus their opposing spins cancel each other out, and the material eventually would not display any magnetism. Conversely, if there are more Fe^{3+} in one site compared to the other, the cancellation would not be perfect, and the material would display some magnetism.[22]

It is expected that the magnetic properties of Al-doped zinc ferrite to change with increasing concentrations of aluminum. Al^{3+} is nonmagnetic, this means when Al^{3+} replaces Fe^{3+}, the reduction of iron will lead to lowering the magnetization.

3. Methodology

3.1. Starting Materials

Table 1 List of chemicals used in the Pechini synthesis

Compound	**Formula**	**Purity**	**Manufacturer**
Zinc nitrate hexahydrate	$Zn(NO_3)_2 \cdot 6H_2O$	≥99.0%	Sigma Aldrich
Iron-(III) nitrate nonahydrate	$Fe(NO_3)_3 \cdot 9H_2O$	≥98.0%	Sigma Aldrich
Aluminum nitrate nonahydrate	$Al(NO_3)_3 \cdot$ 9H2O	p.a.	Fischer Scientific
Citric acid monohydrate	$C_6H_8O_7 \cdot H_2O$	p.a.	Fischer Scientific
1,4-Butanediol	$C_4H_{10}O_2$	≥99%	Fischer Scientific

3.2. Material Synthesis

The metal nitrates were dissolved in distilled water and stirred continuously. The temperature was then raised to 50 °C. The metal ions were chelated using citric acid at a molar ratio of twice the amount of cations. The solution was maintained at 50 °C while stirring for 30 minutes.

For polycondensation, 1,4-butanediol was added at a molar ratio of four times the amount of cations. The temperature was subsequently increased to 80 °C, and the mixture was stirred for another 30 minutes. The precursor amounts were calculated to yield 5 g of the final product.

The temperature was then raised to 300 °C to facilitate evaporation. After a few hours, the resulting material formed a resilient resin, which was transferred to porcelain crucibles and calcined at 600 °C for 2h.

The calcined product was then ground into a fine powder using a mortar and pestle. To fabricate the ceramics, the powder was pressed into pellets and sintered. Each pellet was made from approximately 0.240 g of calcined powder, using pressing tools with an 8 mm diameter and applying a force of approximately 30 kN. Finally, the pellets were transferred to ceramic crucibles and sintered at 1200 °C for 6h.

3.3. Preparation of the Electrodes

Slurry Preparation

The calcined powders were used to prepare the slurry, along with polyvinylidene fluoride (PVDF) as a binder (provided as a 10% solution in N-Methyl-2-pyrrolidone (NMP)) and carbon black. These three components were mixed in an 80:10:10 weight ratio. Additionally, 2 mL of NMP was added to the mixture, which was then stirred overnight to ensure uniform dispersion.

Sheet Preparation

The resulting slurry was coated onto 25 μm-thick titanium foil in a 200 μm-thick layer. The coated sheets were then dried at 80 °C for approximately 6 hours to remove excess solvent.

Final Electrode Preparation

Once dried, the sheets were punched into 12 mm electrodes. A final drying step was performed under vacuum at 110 °C for 12 hours to eliminate any remaining solvent residues.

3.4. Swagelok Cells

Swagelok cells for the cyclic voltammetry and galvanostatic cycling were made from the previously made cathodes. The anode was chosen to be zinc foil of 100 μm thickness and d = 12 mm. Both negative and positive electrodes were separated by a Whatman GF-D separator with a diameter of d = 13 mm. The separator has been wetted with 130 μl of 3M zinc triflate electrolyte. The reference used was a zinc reference, that was also separated by Whatman separator (d = 8 mm) and wetted by 60 μl of the 3M zinc triflate electrolyte.

3.5. Coin Cells

Coin cells for measuring ionic conductivity were made from the sintered ceramic samples. The ceramics were set up between two (d = 8 mm) Whatman separators, that were wetted by 10 μl of 3M zinc triflate solution. The ceramics were enclosed in non-ionically conducting stainless steel casings.

4. Characterization

4.1. X-ray Diffraction

X-ray diffraction (XRD) is a crucial technique for characterizing crystal structures by analyzing how X-rays interact with their structure. When X-rays encounter a crystal, atoms can scatter the radiation. If the scattered waves are coherent, meaning the scattered X-rays from the atoms and from the incident beam are in phase, then they interfere in a constructive way, which results in a detectable diffraction beam. The scattering follows Bragg's law, which relates the wavelength of the incident X-rays to the nature of the crystalline sample. This allows the determination of the structural properties of the sample.[33]

Bragg's law can be described by the following equation,

$$\boldsymbol{n\lambda = 2d'\sin\theta}. \qquad \text{Eq. 8}$$

where:
n: is order of reflection and is equal to the number of wavelengths in the path difference between diffracted X-rays from adjacent crystal planes
λ: Wavelength of the incident X-rays
d: interplanar spacing
θ: the angle at which X-rays are diffracted by the crystal lattice planes

To analyze the samples, the produced sintered samples were crushed in mortar and scanned for the duration of 3 h and at a 2θ range of 10°– 120° using The Bruker D8 Advance that operates with nickel-filtered Cu-Kα radiation (λ = 1.5405 Å).

4.2. μ-XRF

Micro-X-ray fluorescence (*μ*-XRF) is a non-destructive analytical method to determine the elemental composition of bulk material, it covers a broad range of elements in different weight fraction ranges, from pure to trace elements.[34]
The X-ray beam would strike a sample and cause excitation in the material. This results in electrons getting knocked out from the inner shells of the atoms and the creation of vacancies, when electrons with higher energy orders, fall into these vacancies, a fluorescent X-ray is emitted. The wavelengths and energy of these X-rays are measured to identify and quantify the elements present in the sample. [34]

For this measurement, the (*μ*-XRF, M4 Tornado, Bruker, USA) with a rhodium target in the X-ray tube, connected to a polycarpellary lens and with a maximum power of 30 W, was used. The X-ray tube was operated at a voltage of 50 kV and a current of 600 µA for a measurement time of 10 ms per point to measure the twelve statistically distributed measurement points.

4.3. Density

One of commonly used methods to measure density is the Archimedes method. It a particularly appealing method for its simplicity as well as low-cost methods. The Archimedes principle states that the magnitude of a buoyant force on an object equals the weight of the fluid displaced by the object.[35]
The measuring principle is done through measurement of the mass in air as well as in a fluid. The calculation of the density will be done through the following equation[36],

$$\boldsymbol{\rho}_{\mathbf{s}} = \frac{\boldsymbol{m}_{\mathbf{a}}}{\boldsymbol{m}_{\mathbf{a}} - \boldsymbol{m}_{\mathbf{fl}}} \cdot \boldsymbol{\rho}_{\mathbf{fl}} \qquad \text{Eq. 9}$$

where
ρ_s: sample density
m_a: sample mass in air
m_{fl}: sample mass in fluid
ρ_{fl}: fluid density (temperature dependent)

The sintered ceramic sample were measured in air and then in water. The measurement was done at least 6 times for each pellet. The used scale was from the company Sartorius.

From the X-ray diffraction data, the theoretical density can be determined through the following formula[37],

$$\boldsymbol{\rho}_{\mathbf{XRD}} = \frac{\boldsymbol{Z} \cdot \boldsymbol{A}}{\boldsymbol{V}_{\mathbf{c}} \mathbf{N}_{\mathbf{a}}} \qquad \text{Eq. 10}$$

Where
Z: number of atoms associated with each unit cell
A: atomic weight
V_c: volume of the unit cell
N_A: Avogadro’s number

4.4. Scanning Electron Microscopy

Scanning electron microscopy (SEM) can image and analyze bulk specimen, the primary function is to enlarge small features or object that are too small to be perceptible by the human eye. It does this by scanning an electron beam of high energy on the sample surface this is why it is referred to as scanning electron microscopy.[38]

By applying an electron beam, electrons hit the sample and interact with the material, producing different signals, including secondary electrons, back scattering electrons and X-ray or transmitted electrons. The signals are collected by the detector. The detected signal determines how bright each corresponding point appears on the screen, creating an image based on the electron signal distribution. A stronger signal results in a brighter spot on the display. This process produces a detailed intensity map of the sample's surface. Through the detection of emitted X-rays of the sample, an analysis of the elemental composition is possible.[39]

The ceramic samples were attached on the sample holder with adhesive tape and then sputtered with a thin gold layer. Coating with gold is a normal process to reduce charging effects during imaging and to receive good imaging results. The SEM measurement was done to determine the grain size the different compounds. The instrument used was Phenom XL SEM desktop. The length through the bigger diameter of 100 grains were measured using ImageJ software.

4.5. Electrochemical Impedance Spectroscopy

Electrochemical impedance spectroscopy (EIS) is a method of characterizing the electrical properties of materials and their interfaces. It can be used to observe the dynamic of bound and mobile charge in the bulk or interfacial area of various solids or liquids.[40]

The general approach for EIS analysis is the application of an alternating electrical stimulus, either a known voltage or current to excite the electrochemical system at different frequencies. By measuring the system's response (current or voltage) to this electrical stimulation, a transfer function can be calculated which is the electrochemical impedance of the system.[41]

The main purpose of EIS measurements is to model the tested electrochemical system using equivalent electrical circuits composed of resistors, capacitors, and inductors. Depending on the elements included in the electrical circuit that is tested and the way that they are connected to each other, the impedance will differ.[42]

Since impedance measurements generate numerical results, graphical inspection makes it easier to identify the different circuit elements. However, graphical representations alone are insufficient. Mathematical modeling and curve fitting are necessary to accurately extract circuit parameters. The most common graphical representation of EIS data is the Nyquist and Bode plots.[43]

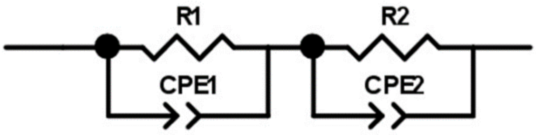

Figure 2 Equivalent circuit

In ceramic materials, the constant phase element (CPE) is often included in equivalent circuit models to account for deviations from ideal capacitive behavior due to structural inhomogeneities, such as variations in grain size and grain boundary effects. The CPE provides a flexible representation of the impedance, allowing for a better fit to experimental data and enabling the separation and analysis of bulk and grain boundary contributions.[44] The used equivalent circuit is seen in figure 2, The R1 and CPE1 represents the bulk, and R2/CPE2 represents the grain boundaries.

The measurements were carried out on an Autolab M204 potentiostat/galvanostat with FRA32M module (Metrohm AG, Switzerland) and the associated software NOVA 2.1.4., for the evaluation of the results the RelaxIS3 software was used with the integrated Nyquist plot and the previously mentioned equivalent circuit.

4.6. Reflection Spectroscopy

One of the most basic methods of characterizing the physical and chemical properties of matter is their interaction with light. Spectroscopy is a widely used method to measure the intensity of transmitted and reflected light.[45]

Reflection describes the event of an electromagnetic radiation being bounced back at the interface between two media. There are different forms of reflectance to be distinguished. The regular specular reflectance. And the diffuse or irregular reflectance. Specular reflection describes a mirror like reflectance, this means that the reflected light exists at angle that is equal to the angle of incidence, this happens in highly polished surfaces. Diffuse or also called remission reflection describes the event where light reflected by the sample is scattered uniformly in all directions, this is due to the roughness of the reflecting surface. This is common in powder samples, ceramics, and nanostructured surfaces, the reflectance from the sample is compared with a standard of known diffuse reflectance.[46]

The spectra will be used to construct Tauc plots of $(F(R)\cdot h\nu)^n$ against photon energy to help in the determination the optical band gap. The band gap is found by extrapolating the linear part of the curves and intersecting with the energy axis.[47]

The Edinburgh Instruments FS920 spectrometer combined with a Teflon-coated integrating sphere was used to analyze the reflection. The Xe900 arc lamp from Edinburgh Instruments with 450 W and a R928 detector from Hamamatsu, Peltier-cooled to -20 °C, were used for the measurement. The rays are guided through the spectrometer via a lens optic. Measurements were initially taken in the wavelength range from 250 nm to 500 nm with a step size of 1.0 nm and then from 480 nm to 800 nm with a 455 nm filter and a step size of 1.0 nm. Both spectra were then combined at 490 nm. Barium sulfate (BaSO4; 99.99%; Sigma-Aldrich 2333.38 g/mol) was used as the reflection standard.

4.7. Cyclic Voltammetry

Cyclic voltammetry (CV) is one of the most common electrochemical techniques used to investigate the oxidation and reduction processes of an electrochemical system. Cyclic voltammetry is a potential sweep method, the potential at which no current flows is set as the starting potential then the potential is scanned at a constant rate until reaching the set limit, the voltage is then swept in the reverse direction of the starting point. The data is represented in a cyclic voltammogram, it provides information's about the reactions near the electrode surface and the reactivity of the electrochemically active species.[48]

A three-electrode step-up is used usually for cyclic voltammetry experiments. The three electrodes consist of a working electrode (WE), counter electrode (CE) and a reference electrode (RE). The (WE) carries out the chemical reaction of interest, a potentiostat is used to control the applied potential of the working electrode as a function of the reference electrode potential. The RE has a known and stable equilibrium potential, it's used as reference against which the potential of other electrodes can be measured. For this reason, the potential is recorded as "vs" the used reference. When a potential is applied to the WE to induce a reaction, a current starts to flow, the CE completes the circuit, allowing the electrons to transfer between the WE and CE and the resulting current is recorded.[49]

For this measurement, Swagelok cells were investigated with an Autolab M204 potentiostat/galvanostat (Metrohm AG, Switzerland). The potential window was between 0.8 V and 1.7 V against Zn/Zn^{2+} reference at a scan rate of $v = 0.2\ mV.s^{-1}$.

4.8. Galvanostatic Cycling

Galvanostatic charge and discharge (GCD) technique records the voltage between the WE and RE of a system under the application of a constant current. It is the most common way of determining the capacity, reversibility, stability and rate capability of an electrochemical system. By repeatedly charging/discharging batteries one can evaluate the cycle life, which is often referred to the cycle number at which the reversible capacity fades to 80% of its initial value. For GCD the terminal voltage needs to be determined at which the current direction will be inverted.[50]

GCD data are plotted as potential vs time, capacity or specific capacity. The curves can suggest the primary charge storage mechanism. Systems that store energy by faradaic charge storage mechanism will show one or more GCD plateaus at the potentials associated with the electrochemical redox reaction. Meanwhile systems with mixed capacitive and faradaic charge storage mechanism can have either a sloping charge/discharge curves or triangular-like shapes in E vs time curves. The particle size of the electroactive material can also have an influence on the shape of the Charge/discharge curves.[51]

Swagelok cells were used for GCD testing, they were performed at a Maccor series 4000 battery tester (Maccor Inc., Oklahoma, USA). The cells were cycled in a voltage range of 0.7 and 1.8 V vs. Zn/Zn^{2+} with 0.1C.

4.9. AFM

Atomic force microscopy (AFM) is a scanning probe microscopy technique for high resolution imaging of conducting as well as non-conducting surfaces. The key measured property in AFM is the interaction force between the probe tip and the surface of the sample.[52]

In AFM there are three types of imaging modes of the sample surface: contact, tapping and non-contact mode:
Contact mode: the probe tip is always in contact with the sample, the surface structure is obtained from the defection of the cantilever.
Tapping mode: the probe does not stay in constant contact with the sample but taps the surface; by looking at the probe's vibration change during the tapping motion this enables learning about the probe's surface structure.
Non-contact mode: the probe never contacts the sample surface but instead it moves very close to the surface of the sample, and by measuring the probe's vibration change due to the surface influence one can establish information about the surface structure.[52], [53]

Kelvin probe force microscopy (KPFM) is a technique that is based on non-contact AFM. It works by applying a dc-voltage to balance out the potential difference (CPD) between the probe and the sample, KPFM measures the electrostatic force between the probe and the sample. KPFM applies a feedback loop that adjust the voltage until the forces are canceled out. The final voltage gives information about the work function of the sample compared to the tip of the probe.[54]

The instrument used for this measurement is Cypher ES (Oxford Instruments, UK) with Pt coated cantilevers (PPP-NCSTPt by Nanosensors).

4.10. NIR-Emission Spectroscopy

Luminescence is the emission of ultraviolet visible or infrared photons from an electronically excited species in non-thermal equilibrium, thus not incandescence or Planck radiation. Luminescence can be classified according to the type of excitation mode. Two cases of photoluminescence are fluorescence and phosphorescence, for both the mode of electronic excitation is through the absorption of a photon. The subsequent emission of light as the species return to a low energy state is called photoluminescence which results from the interaction of light with matter. [55]

The measurement is conducted with a spectrofluorometer. A light beam from a lamp or laser passes through a filter or monochromator to isolate the desired excitation wavelength before reaching the sample. The sample absorbs this light and emits fluorescence in all directions. The emitted fluorescence then passes through another wavelength selector before reaching a photodetector, which converts it into an electrical signal. A reference beam, attenuated before reaching a second photodetector, monitors excitation intensity. The system compares the fluorescence signal to the reference beam for accuracy, and the collected data generate the spectra. [56]

Some of the photoluminescence spectra that can be obtained are excitation spectra by measuring luminescence intensity at a fixed wavelength while the excitation wavelength is varied. This is usually the first step in determining the optimal excitation conditions. Meanwhile fluorescence and phosphorescence spectra are generated by exciting the sample at a fixed excitation wavelength while recording the emission intensity as a function of the wavelength.[56]

The Edinburgh Instruments FSL 920 Fluorescence spectrometer with Xe900 arc lamp (Edinburgh Instruments) with single photon PMT detector from Hamamatsu R2658P (red, cooled), were used for the measurement. In addition, a TMS300 monochromator is installed on the excitation and emission sides. The sintered ceramic samples were crushed into powder and used for this analysis.

4.11. Magnetic Susceptibility

Magnetic susceptibility (MS) measurements are the first characterization technique to turn to for assessing an unknown material’s magnetic nature. MS is the physical quantity describing a material’s properties in an external magnetic field.[57]

There are different techniques for measuring the magnetic properties of substances, they rely on their interaction with an external magnetic field. These methods typically measure either the force exerted on a sample in an inhomogeneous field or changes in magnetic flux density when the sample is placed in a magnetic field.[58]

One method of measuring the MS of a material is using the Evan’s balance. The working principle is two small permanent magnets are supported by a suspension strip. The force that the sample exerts on one of the magnets is balanced by a current through a coil placed between the poles of the other magnet. The current measured through the coil is proportional to the force exerted by the sample.[59]

The instrument used for these measurements is a JM Auto Magnetic Susceptibility Balance, which directly indicates material’s volume susceptibility. Powder from sintered ceramics was used for these measurements.

5. Discussion

5.1. XRD

To assess the phase purity and to determine the structural properties of the final compounds, powder x-ray diffraction technique was employed. The XRD patterns for all the fabricated compositions of $ZnFe_{2-x}Al_xO_4$ are illustrated in figure 3.

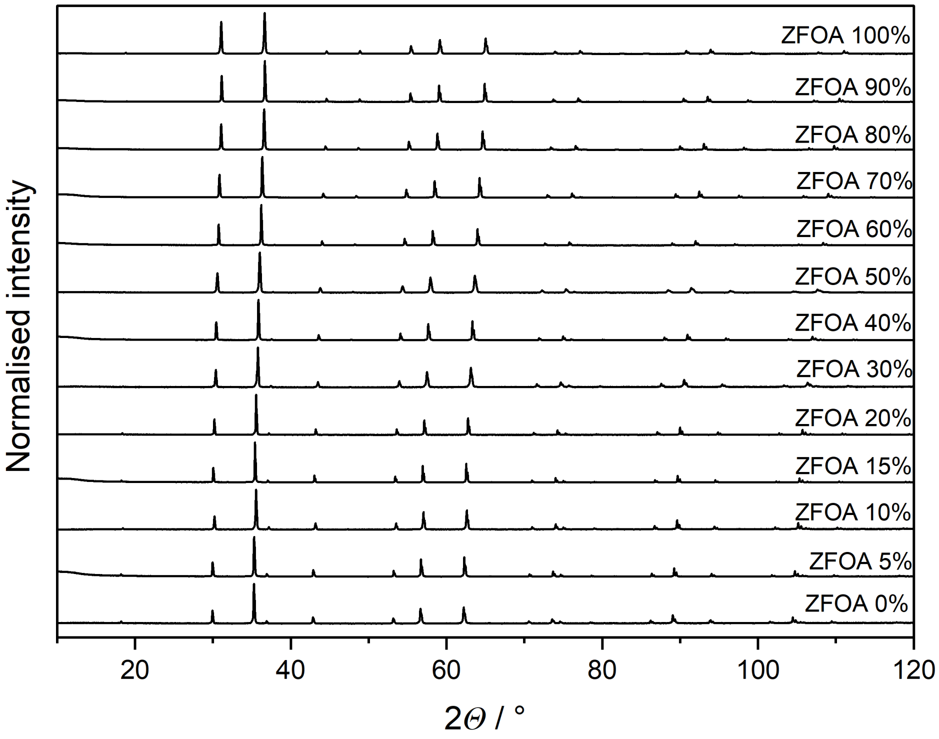

Figure 3 XRD patterns of $ZnFe_2O_4$ - $ZnAl_2O_4$

From inspection of the XRD patterns of $ZnFe_{2-x}Al_xO_4$, they match well with the standard reference data [60], the most prominent diffraction peaks, consistent across all compounds, appear at a 2θ value ranges (from the lowest to the highest Al^{3+} content) as follows: [29.90°-31.16°], [35.31°-36.56°], [42.85°-44.29°], [56.72°-59.07°], [62.12°-65.18°], which correspond to the hkl planes (220), (311), (400), (511), (440) respectively. These reflections are characteristic of the cubic spinel structure. The rest of the peaks can also be identified and assigned their respective Miller indices.

The absence of any additional unknown peaks indicates that the aluminum ions have been successfully incorporated into the structure, and no secondary phases were generated upon Al^{3+} incorporation. This confirms that the compounds are of single phase and suitable for further characterization.

To investigate how the incorporation of aluminum ions affects the cubic structure, the lattice parameter (a) was calculated for each compound using the following equation:

$$a = d.\sqrt{h^2 + k^2 + l^2} \qquad \text{Eq. 11}$$

where a is the lattice parameter (Ǻ), d is the distance between adjacent planes (Ǻ) and hkl are the Miller indices.

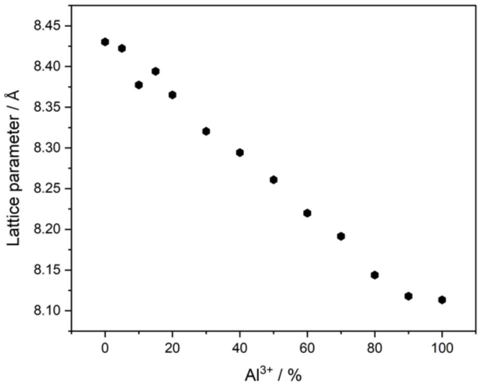

Figure 4 Lattice parameter vs Al^{3+} content in %

Table 2 Lattice parameter at different Al^{3+} concentrations

Al^{3+} content (%)	**a (Ǻ)**
0	8.430
5	8.422
10	8.377
15	8.394
20	8.365
30	8.320
40	8.294
50	8.261
60	8.220
70	8.192
80	8.144
90	8.118
100	8.113

The calculated lattice parameters range from the maximum value of 8.430 Ǻ (for the compound with 0% Al^{3+}), which is consistent with the values from literature [60] to a minimum value of 8.113 Ǻ (for the compound with 100% Al^{3+}). This reflects a general decreasing trend as the Al^{3+} content increases. This decrease in the lattice parameter can be attributed to the smaller ionic radius of aluminum (0.53 Ǻ, [61]) compared to iron (0.65 Ǻ, [61]). If the radius of the substituted ion is larger than the displaced ions, the lattice shrinks and as a result the lattice constant decreases.

Furthermore, the peaks shift to a higher 2θ angle as Al^{3+} increases, further confirming the lattice contraction resulting from the substitution of the larger iron ions with the smaller aluminum ions. This shift indicates a decrease in the interplanar spacing and the overall contraction of the unit cell due to incorporation of aluminum ions.

5.2. *μ*-XRF

μ-XRF measurements were conducted to determine the real composition in each compound. *μ*-XRF cannot detect elements with low atomic numbers due to the weak X-rays they produce. Therefore, it was not possible to quantify the oxygen content. Accurately measuring the aluminum was also difficult. However, iron and zinc can be detected properly. Therefore, for the determination of the final composition, the zinc and iron content were calculated directly from the *μ*-XRF data, while the aluminum and oxygen amounts were merely estimated.

The resulting compositions for the final compounds are listed in table 3:

Table 3 Actual compositions of the produced compounds

The planned composition	**The actual composition**
$ZnFe_2O_4$	$Zn_{1.05}Fe_{1.95}O_4$
$ZnFe_{1.9}Al_{0.1}O_4$	$Zn_{1.04}Fe_{1.86}Al_{0.1}O_4$
$ZnFe_{1.8}Al_{0.2}O_4$	$Zn_{1.06}Fe_{1.74}Al_{0.2}O_4$
$ZnFe_{1.7}Al_{0.3}O_4$	$Zn_{1.03}Fe_{1.67}Al_{0.3}O_4$
$ZnFe_{1.6}Al_{0.4}O_4$	$Zn_{1.06}Fe_{1.54}Al_{0.4}O_4$
$ZnFe_{1.4}Al_{0.6}O_4$	$Zn_{1.07}Fe_{1.33}Al_{0.6}O_4$
$ZnFe_{1.2}Al_{0.8}O_4$	$Zn_{1.07}Fe_{1.13}Al_{0.8}O_4$
$ZnFeAlO_4$	$Zn_{1.07}Fe_{0.93}Al_1O_4$
$ZnFe_{0.8}Al_{1.2}O_4$	$Zn_{1.07}Fe_{0.73}Al_{1.2}O_4$
$ZnFe_{0.6}Al_{1.4}O_4$	$Zn_{1.07}Fe_{0.53}Al_{1.4}O_4$
$ZnFe_{0.4}Al_{1.6}O_4$	$Zn_{1.06}Fe_{0.34}Al_{1.6}O_4$
$ZnFe_{0.2}Al_{1.8}O_4$	$Zn_{1.04}Fe_{0.16}Al_{1.8}O_4$
$ZnAl_2O_4$	$ZnAl_2O_4$

5.3. Density

The bulk density, theoretical density, relative density and porosity were calculated for each compound. In ceramics, the porosity is an important property as it has direct influence on the final properties of the ceramics. It effects the electrical properties, optical behavior, can reduce the mechanical strength as well as allow permeability of liquids and gases. [62]

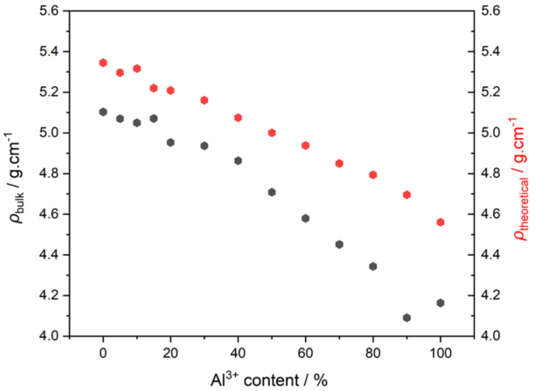

Figure 5 Bulk and theoretical densities vs Al^{3+} content

Table 4 presents all the above-mentioned physical properties of all the compounds:

Table 4 Bulk, theoretical, relative densities and porosity of all $ZnFe_{2-x}Al_xO_4$ compounds

Al^{3+} content (%)	ρ_{bulk} (g/cm^3)	$\rho_{theoretical}$ (g/cm^3)	$\rho_{relative}$ (%)	Porosity (%)
0	5.10	5.35	95.48	4.52
5	5.07	5.30	95.72	4.28
10	5.05	5.32	94.98	5.02
15	5.07	5.22	97.15	2.85
20	4.95	5.21	95.08	4.92
30	4.94	5.16	95.66	4.34
40	4.86	5.07	95.83	4.17
50	4.71	5.00	94.15	5.85
60	4.58	4.94	92.75	7.25
70	4.45	4.85	91.80	8.20
80	4.34	4.79	90.62	9.38
90	4.09	4.70	87.12	12.88
100	4.16	4.56	91.30	8.70

As it can be derived from figure 5 the theoretical density decreases with increasing Al^{3+} content, this can be explained by the fact that aluminum atoms have a lower density and atomic weight compared to iron atoms.

The bulk density displays a similar trend to the theoretical density due to the replacement of Fe^{3+} with Al^{3+}. It is also worth mentioning that the bulk density generally exhibits lower values than the theoretical density. This discrepancy is likely due to the presence of pores that form during the pressing of the pellets.

When examining the relative density values, on the one hand one can see that the compounds with aluminum content ranging from 0% to 40% displayed a 95% or higher relative density which is desirable for ceramics.
On the other hand, the compounds with aluminum content ranging from 50% to 100% show a general decrease in the relative density (indicating a higher porosity) as the aluminum content increases.

Another possible reason for increased porosity in the compounds with higher aluminum content could be related to the sintering conditions. Specifically, the compounds with higher Al^{3+} content may require a higher pressure when pressing into pellets or higher sintering tempertures to reduce any pores and ensure proper grain growth, ensuring a more uniform and dense ceramic structure.

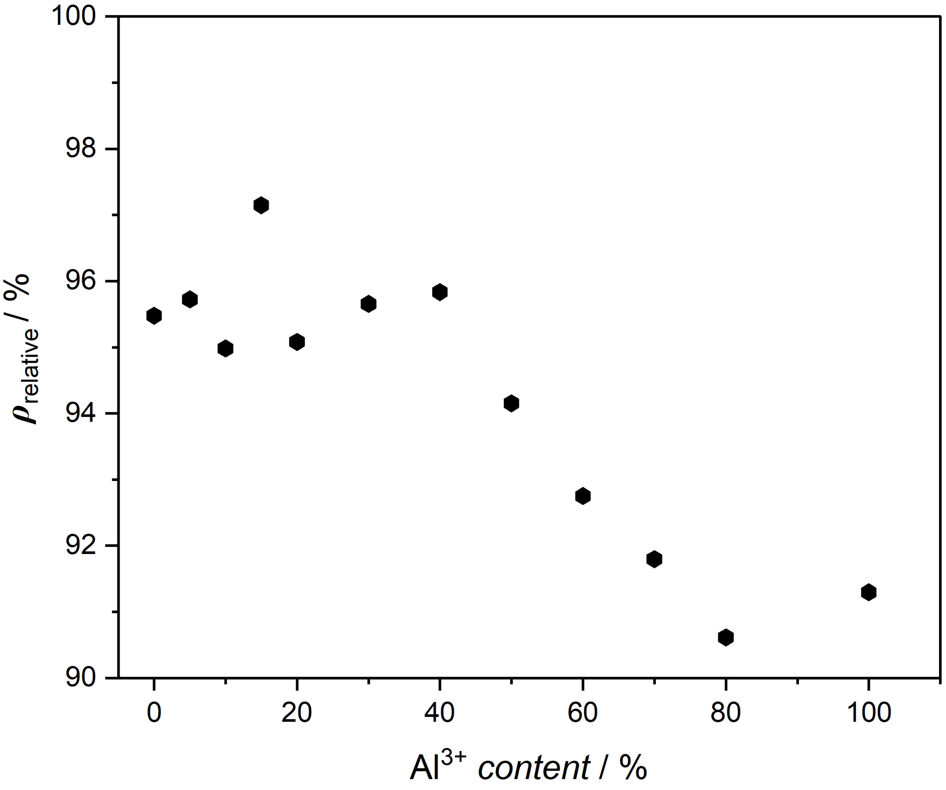

Figure 6 Relative densities vs Al^{3+} content

5.4. Grain Size

SEM was used to observe the change of the grain size as well as appearance of the different compounds with varying aluminum concentration. The grain size determination is an important microstructural feature of the properties of ceramics. Determining the grains size gives an idea about the concentration of the grain boundaries. [63], [64]

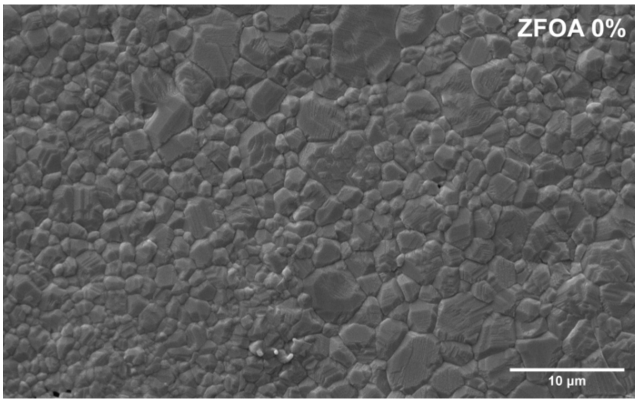

Figure 7 SEM image of pure zinc ferrite

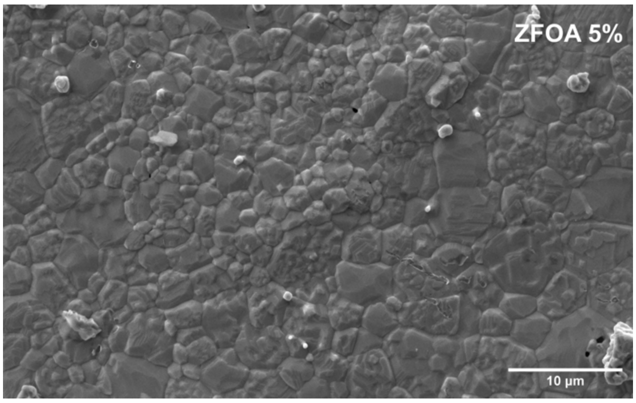

Figure 8 SEM image of 5% Al-doped zinc ferrite

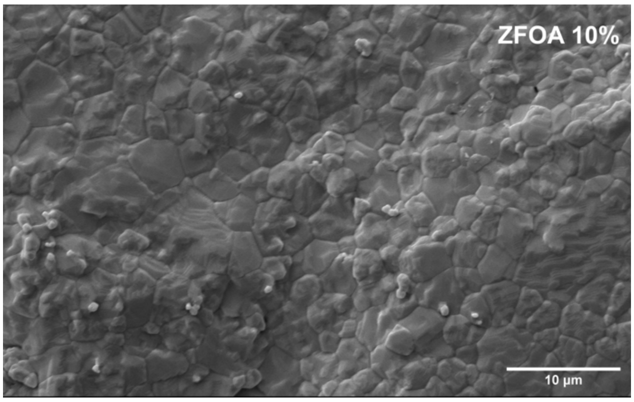

Figure 9 SEM image of 10% Al-doped zinc ferrite

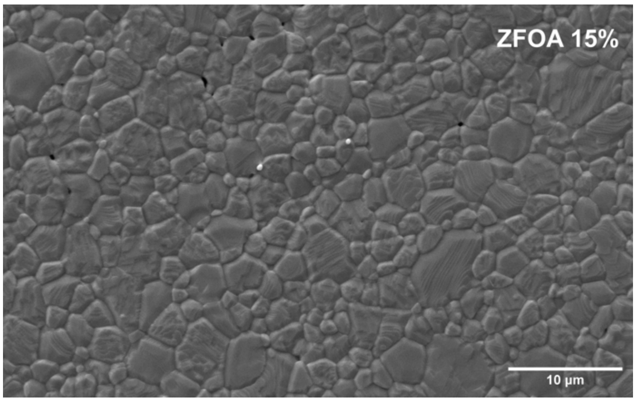

Figure 10 SEM image of 15% Al-doped zinc ferrite

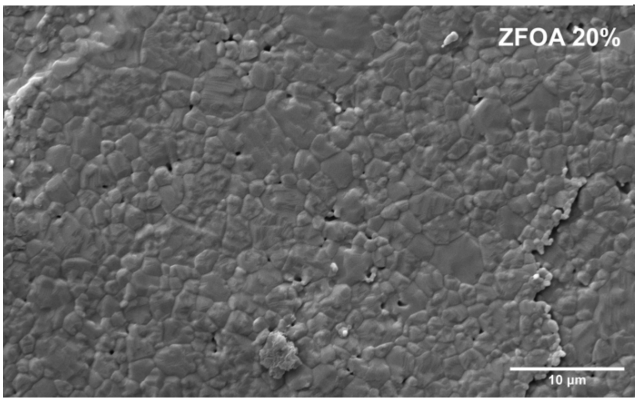

Figure 11 SEM image of 20% Al-doped zinc ferrite

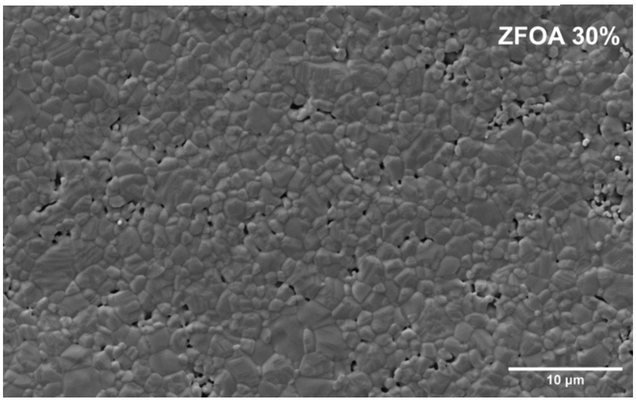

Figure 12 SEM image of 30% Al-doped zinc ferrite

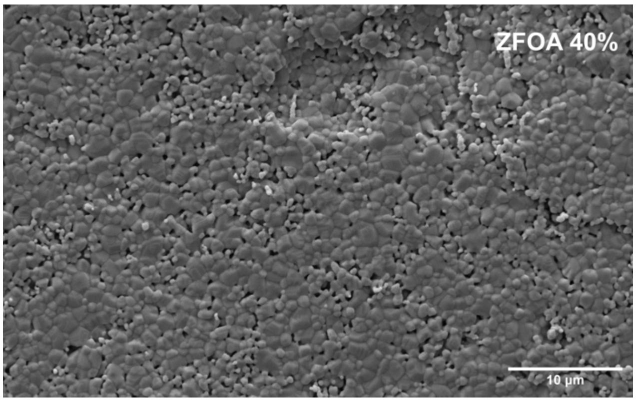

Figure 13 SEM image of 40% Al-doped zinc ferrite

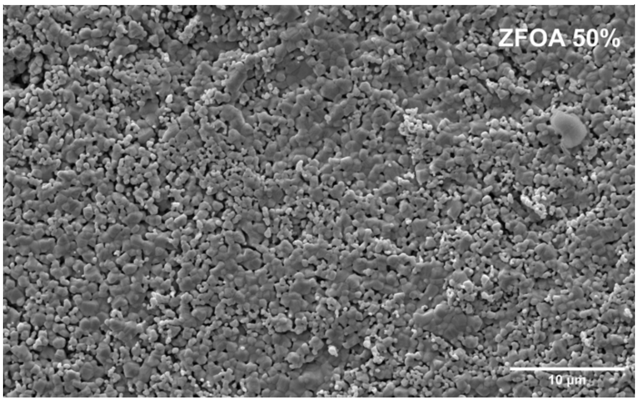

Figure 14 SEM image of 50% Al-doped zinc ferrite

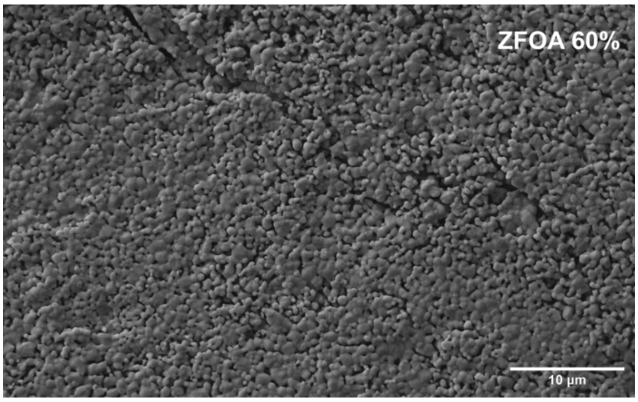

Figure 15 SEM image of 60% Al-doped zinc ferrite

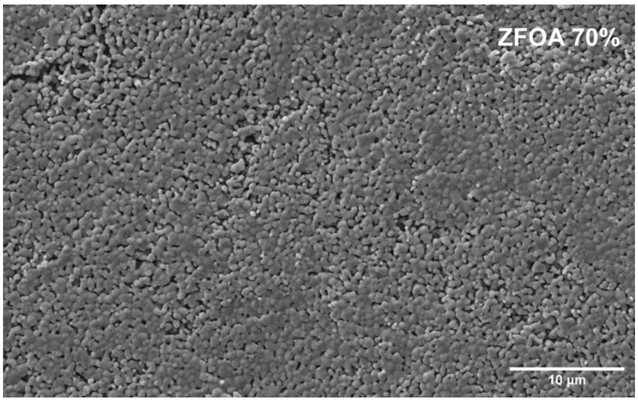

Figure 16 SEM image of 70% Al-doped zinc ferrite

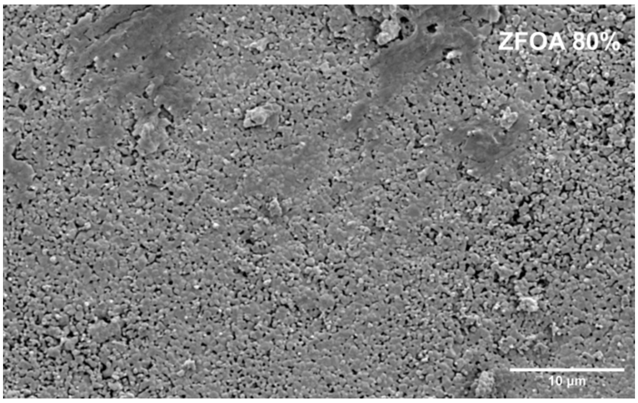

Figure 17 SEM image of 80% Al-doped zinc ferrite

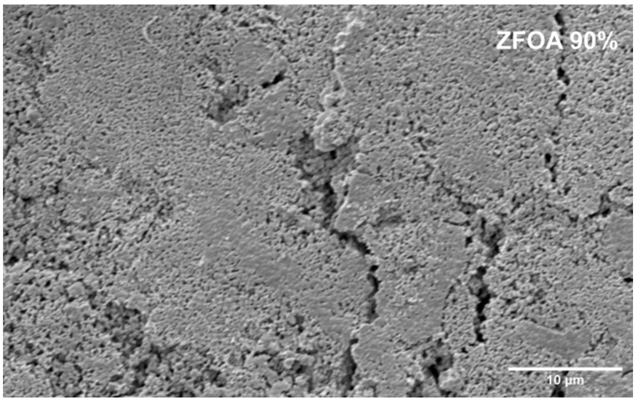

Figure 18 SEM image of 90% Al-doped zinc ferrite

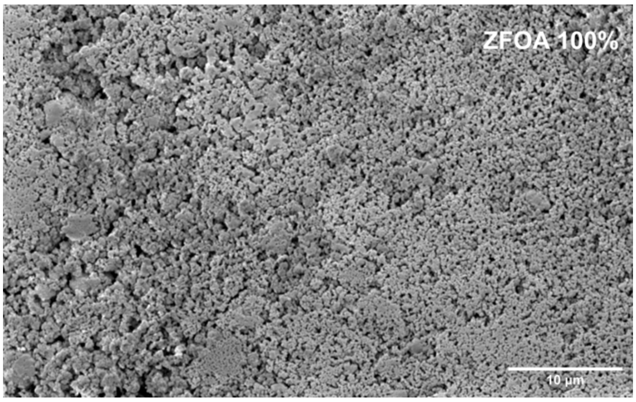

Figure 19 SEM image of pure zinc aluminate

All the SEM pictures were taken using the same magnification, there is a noticeable decrease in grain size accompanying the increase in aluminum content. From the previous pictures it was possible to measure the average size of the grains for each compound except for the compounds with 90% and 100% Al^{3+} content:

Table 5 Average grain size at different Al^{3+} contents

Al^{3+} percentage (%)	Grain size (μm)
0	3.772 ± 1.389
5	3.329 ± 1.349
10	3.250 ± 1.730
15	3.058 ± 1.067
20	2.931 ± 1.132
30	1.804 ± 0.657
40	1.339 ± 0.448
50	0.873 ± 0.351
60	0.765 ± 0.271
70	0.563 ± 0.195
80	0.424 ± 0.176
90	-
100	-

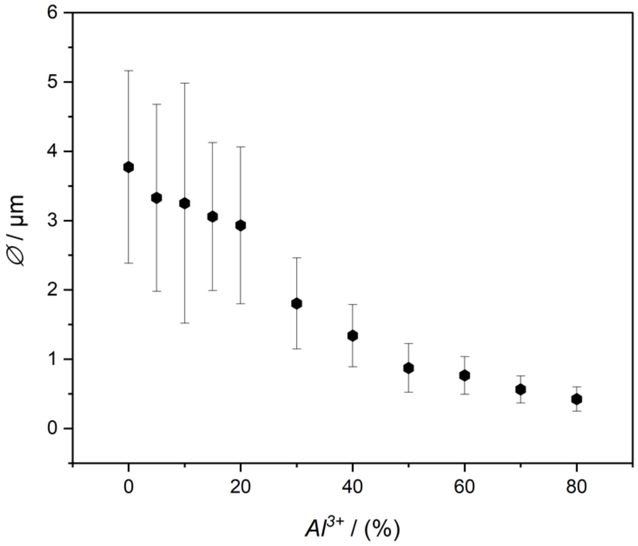

Figure 20 Average grain size vs Al^{3+} content

It was not possible to determine the grain size for the last two compounds due to the small size of the grains.

For the compounds with the aluminum content range 0% - 80%, one can see in figure 20 that there is a trend of decreasing grain size as the aluminum content increases. It is also noticeable from the taken pictures that for the aluminum concentration range of 0% - 40% the grains display high compacted grains with some grains being extremely large compared to others, meanwhile for the concentration range 50% - 100% the grains seem a bit more agglomerated as well as more uniform in size. There is also a noticeable increase in the number of pores with the increase in aluminum content.
The XRD data supports these observations, showing that compounds with higher aluminum content tend to exhibit smaller grain sizes. This suggests that increasing the aluminum content may reduce the final particle size, potentially leading to the formation of smaller grains.

Another factor influencing the grain growth during sintering is presence of pores. Poorly compacted powders result in ceramics with higher number of pores which might inhibit the grain growth, and this might result in smaller grain sizes. The extreme size of some of the grains at lower aluminum content, is referred to as exaggerated grain size, some fraction of the grains grows to a large size consuming the surrounding smaller grains. And once a grain grows to such a size that it has many more sides than the neighbouring grains, the curvature of each side increases, and it grows more rapidly than the smaller grains with fewer sides. [63]

5.5. Conductivity

To investigate the effect of aluminum doping on the electric properties, the total conductivity was measured from the Au sputtered ceramic samples with platinum wires. The measurements were done in only the concentration ranges from 0% to 50% since it was expected that higher aluminum doped compounds would display a very low electrical conductivity.

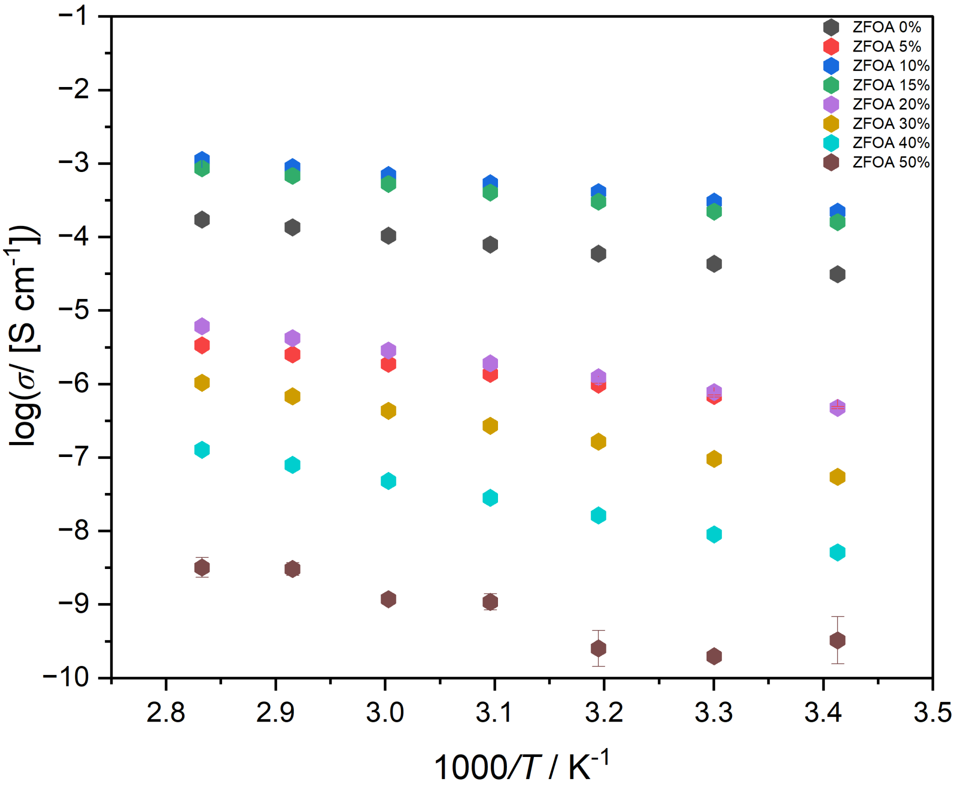

Figure 21 Total conductivity in relation to the temperature

As it can be seen from the figure 21, the ZFOA 10% displays the highest conductivity, followed by ZFOA 15%, which partially overlaps with ZFOA 10%. The pure zinc ferrite ranks next in conductivity, followed by the 5% and 20% aluminum doped compounds. A notable decline in conductivity is observed as aluminum concentrations increase beyond 20%.

As explained previously, the electrical conductivity in zinc ferrite is governed by the electronic conductivity. The electron transport in zinc ferrite happens via electron hopping, where charge transport takes place through the Fe^{2+} and Fe^{3+} redox exchange at the octahedral sites. The decrease in conductivity observed in the ZFOA 5% can be attributed to the substitution of Fe^{3+} by Al^{3+} in the octahedral sites, thus reducing the number of available Fe^{2+}/ Fe^{3+} pairs and thereby limiting electron hopping.

In contrast, the increase in conductivity in the ZFOA 10 % and ZFOA 15% might be explained by a mechanism reported literature for certain Al-substituted ferrites. Studies suggest that at a higher aluminum concentration, Al^{3+} ions progressively occupy the tetrahedral sites, leading to a higher concentration of Fe^{3+} ions in the B sites. This redistribution enhances electron hopping efficiency, thereby improving conductivity.[64], [65]

Finally, the decrease in conductivity in ZFOA 20% and beyond is due to the significant decrease of iron content, which leads to lower Fe^{2+}/Fe^{3+} pairs, thereby reducing of number of charge carriers. The decrease of the grain size would also result in decrease in electrical conductivity, as more boundaries hinder the mobility of the charge carriers.

Additionally, there is also noticeable increase in conductivity at higher temperatures. This behavior can be explained through the increase in the mobility of the charge carriers which are thermally activated through the increase in temperature. The thermal activation of charge carriers is to be expected in semiconductors, and it follows the Arrhenius equation:

$$\boldsymbol{\sigma = \sigma_0 exp\left(\frac{E_a}{k_B.T}\right)} \qquad \text{Eq. 12}$$

where σ is the conductivity, σ_0 is the pre-exponential factor, E_a is the activation energy, k_B is the Boltzmann constant, and T is temperature.

Through the previous equation it was possible to evaluate the activation energies for compound with Aluminum content ranging from 0% to 50%.

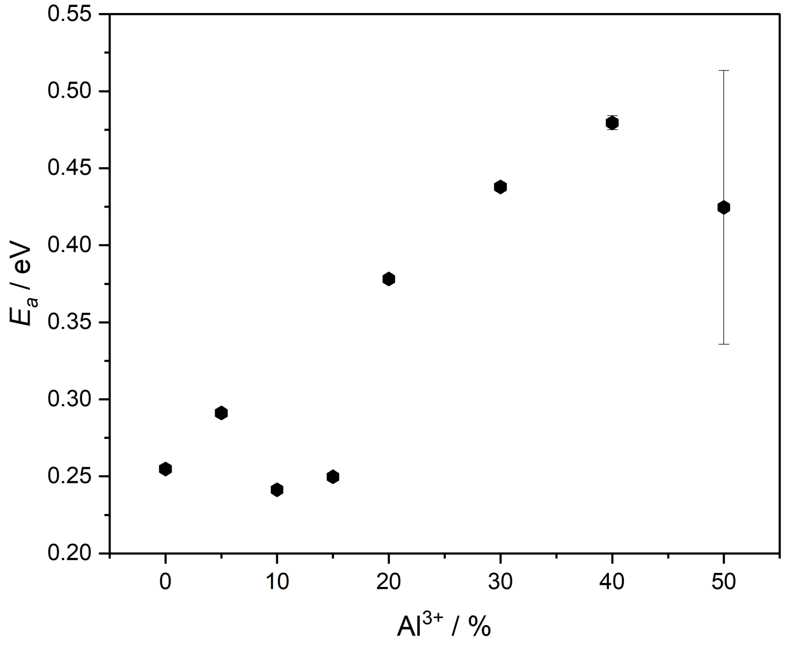

Figure 22 Activation energies vs Al^{3+} content in %

From figure 22 the lowest activation energy belongs to the compound with the 10% Al^{3+} content at a value of 0.24 eV, it is then followed by 15% at a value of 0.24 eV. The values then increase from the pure zinc ferrite to 40% aluminum content. The compound with 50% aluminum is of a lower activation energy compared to the compound with 40% aluminum content, it does however display a large error bar.

Separate measurements of the ionic contribution to the electrical conductivity were conducted in a two-electrode measurement setup with electron-blocking contacts using coin cells. The equivalent circuit to describe the setup consists of a series of three resistors with each a parallel constant-phase-element: one resistor/CPE for the Zn-ion transport in the electron blocking contacts, one resistor/CPE for the Zn-ion transport in the ceramic sample and one resistor/CPE with blocking characteristics for the blocking interface with the metal electrodes.

The first trial entailed the ceramic samples sandwiched between two electrolyte-wetted separators. This turned out to be suboptimal since the conductivity of the samples were highly overestimated (in the mS/cm range), perhaps due to the liquid electrolyte leaking into the pores of the samples and somehow affecting the resistance.

In the second trial, a gelled version of the electrolyte was used, with agar-agar which is a polysaccharide as the gelling agent.

The Nyquist plots from the obtained impedance measurements are as follows:

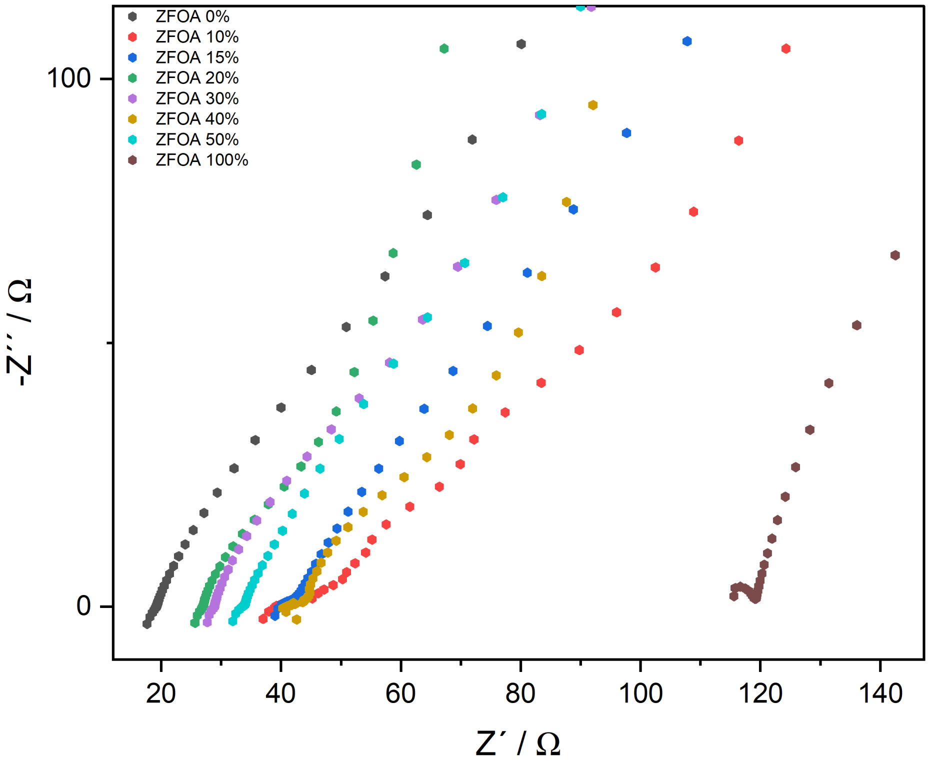

Figure 23 Nyquist plot of different ZFOA compositions at room temperature

As it can be observed, the resistance is quite low, this means that the data are not very reliable when it comes to extracting the exact values of the ionic conductivity, the data from the samples are again overestimated, possibly because of the previously mentioned electrolyte leakage into the pores.

However, based on the Nyquist plot from figure 23, one can make a qualitative observation about the ionic conductivity trends across samples with varying Al^{3+} contents, since the conductivity – even though it is too high – seems to depend on the composition of the ceramic sample. The ZFOA 0% sample is likely to exhibit the highest conductivity, while the ZFOA 100% sample shows the lowest conductivity. The ZFOA 20% and ZFOA 30% samples have intermediate conductivities, ranking just after the pure zinc ferrite. The most electronically conductive samples, ZFOA 10% and ZFOA 15%, lie between the pure zinc ferrite and pure zinc aluminate in terms of conductivity.

Unfortunately, there is no obvious trend to be observed in these results, a better measurement method must be applied to fully understand the effect of Al-doping on zinc ferrite ionic conductive properties.

5.6. Band Gap Determination

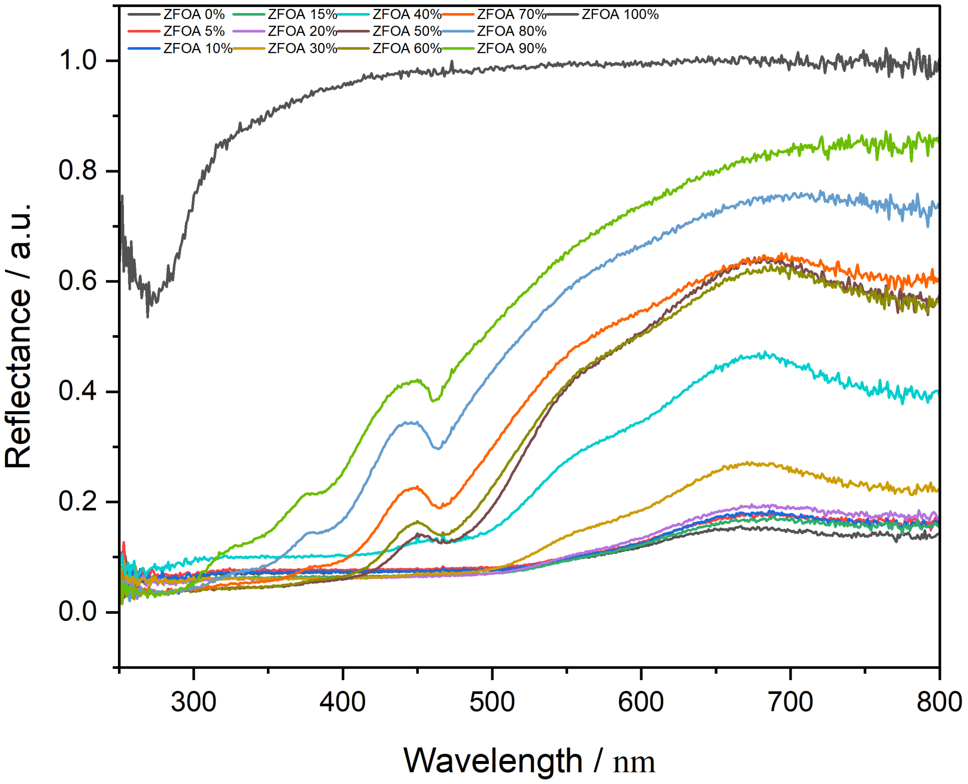

Figure 24 Reflection spectra of $ZnFe_{2-x}Al_xO_4$

The reflection spectra of $ZnFe_{2-x}Al_xO_4$ samples show a clear trend as Al^{3+} replaces Fe^{3+} in the spinel structure. As the Al^{3+} content increases, reflectance gradually rises, indicating a reduction in absorption and a possible widening of the band gap. There is also a slight difference in the reflectance behavior at concentrations from 50% to 90% aluminum content, this is perhaps due to some secondary phases that were not detectable in XRD measurements.

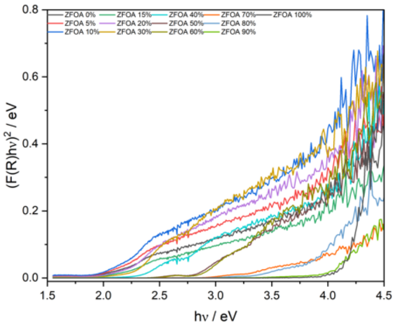

Figure 25 Tauc plots of all compounds

The ZFOA 100% (pure zinc aluminate) exhibits the highest reflectance, indicating minimal absorption and a wide bandgap. In contrast, iron-rich compositions display significantly lower reflectance, suggesting strong absorption in the visible region. This suggests the change from absorbing optical response to more reflective response when increasing the aluminum content.
The reflectance was transformed into the corresponding absorption spectra using the Tauc plot that can be seen in figure 25.

The band gap energy values can be taken from extrapolating to the axis cut off from $(F(R)h\nu)^2$ against the energy ($h\nu$). The results for the band gap energy can be found in table 6.

Table 6 Band gap energy of all ZFOA compounds

Al^{3+} content %	E_g eV
0	2.02
5	2.04
10	2.06
15	2.09
20	2.14
30	2.22
40	2.29
50	2.42
60	2.85
70	2.88
80	3.27
90	3.31
100	4.16

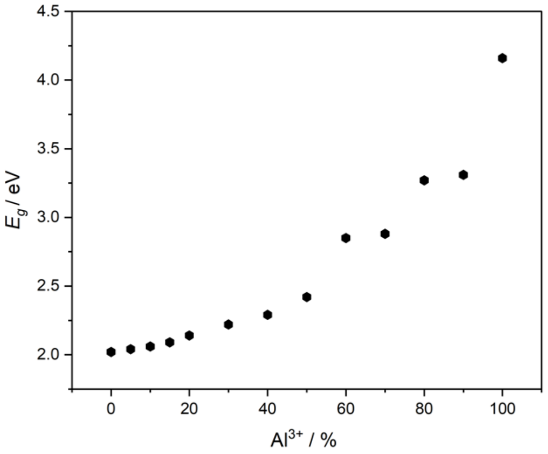

Figure 26 Band gap energy at different Al^{3+} contents in %

As it can be seen the pure zinc ferrite (0% Al^{3+} content) displays the lowest band gap energy at a value of 2.02 eV which agrees with the values from literature [14]. The values then increase with the increase in aluminum content which indicates the widening of the band gap, finally the pure zinc aluminate (100% Al^{3+} content) displays the highest energy band gap at 4.16 eV.

This trend suggests that as the iron ions are substituted from the compounds, the material changes from a semiconducting to more insulating state.

5.7. Cyclic Voltammetry

To gain insight into the electrochemical behavior of the compounds, the concentration range 0% to 50% was investigated using Cyclic voltammetry. CV measurements were conducted to analyze the redox activity, and potential charge storage mechanisms. The CV curves provide valuable information on oxidation and reduction peaks, helping to identify the active redox couples and assess the material's reversibility during cycling.

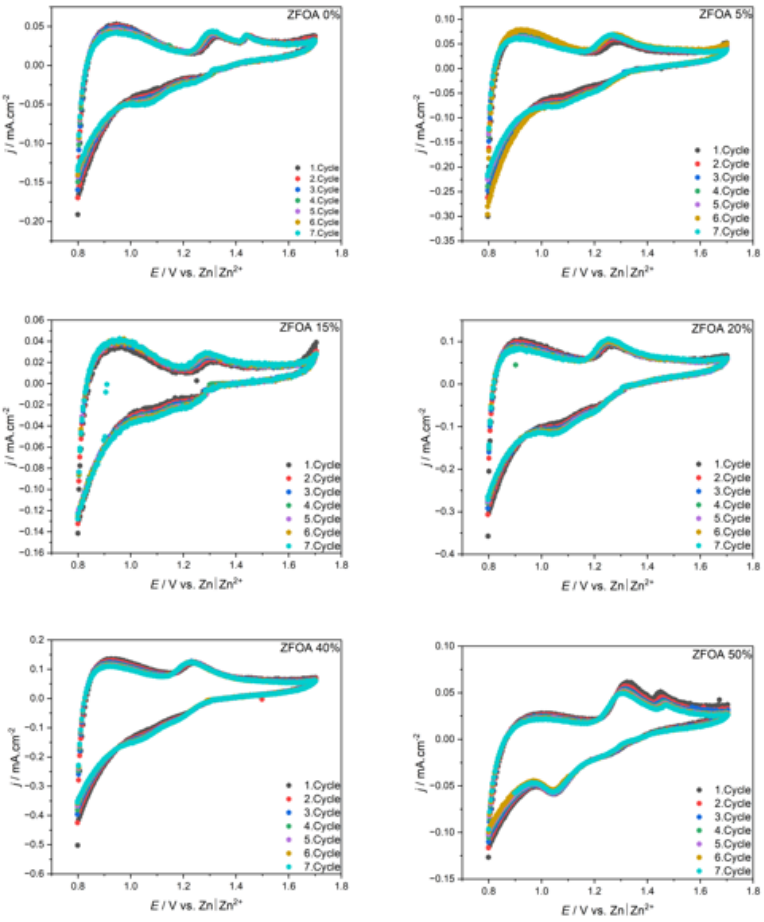

Figure 27 Cyclic voltammetry measurements of ZFOA in the concentration range between 0% and 50% using the positive electrode as working electrode, zinc metal as counter electrode and 3M zinc triflate as electrolyte with a scan rate of 0.2 mV s^{-1} for 7 cycles in a range of 0.8 V 1.7 V vs Zn│Zn^{2+}

The voltammogram for the pure zinc ferrite exhibits characteristic curves typical in battery systems. Two distinct oxidation peaks observed at the voltage range of 1.22 V – 1.41 V for the first peak and 1.41 V – 1.48 V for the second peak.

Additionally, there are two broad and flat reduction peaks that can be observed in the voltage range of 1.31 V – 1.18 V for the first peak and the second peak is approximately in the range of 1.18 – 097 V.

The voltammogram for ZFOA 10%, the most promising material due to the high conductivity displays similar behavior to the pure zinc ferrite. The first oxidation peak appears within the voltage range of 1.21 V - 1.41 V while the second peak is in the voltage range 1.41 V – 1.50 V. Additionally, this curve also displays two flat reduction peaks at voltage ranges of 1.28 V – 1.19 V and 1.12 V – 0.98 V.

The second most promising material ZFOA 15% also displays behavior characteristic of battery system, however there is only one oxidation peak to be observed at the voltage range of 1.21 V – 1.38 V. Additionally, two possible reduction peaks appear in the range of 1.28 V – 1.02 V, although they are noticeably flatter in comparison to the previous curves.

For the rest of the compounds, all except for ZFOA 50% exhibit only one oxidation peak, with the voltage decreasing from the highest range observed for ZFOA 5% at 1.17 V – 1.36 V to the lowest range for ZFOA 40% 1.14 V – 1.34 V. The oxidation peak voltages for these compositions are noticeably lower than those of the previously mentioned compounds. The reduction peaks for these curves are not very prominent.

The ZFOA 50% compound, however, displayed two oxidation peaks and a very prominent reduction peak as well as a very broad and flat reduction peak at a higher potential. The oxidation peaks occur in the voltage ranges of 1.19 V – 1.43 V and 1.43 – 1.51 V which are higher than those of the compounds from 5% – 40%. The prominent reduction peak is observed in the voltage range of 1.09 V – 0.97 V, the second broad and nearly flat reduction peak can be observed at the potential range of 1.2 V – 1.4 V.

The first peaks in the previous voltammograms can be attributed to the deinsertion of Zn^{2+} from the positive electrode and the oxidation of Fe^{2+} to Fe^{3+}.

The second oxidation peak observed in the compounds ZFOA 0% and ZFOA 10% is unexpected but might be due to a second oxidation step, perhaps involving H^+.

Multiple proton storage reaction patterns have been reported in multiple ZMBs related research papers [66], [67], [68]

There are multiple possible mechanisms in this process, the first possible mechanism is the Zn^{2+}/H^+ co insertion, this can happen in three forms, either the H^+ insertion is followed by Zn^{2+} insertion, or Zn^{2+} insertion is followed by H^+ insertion or the simultaneous H^+ and Zn^{2+} happening at the same time.

The second mechanism is H^+ insertion reaction, in this mechanism the H^+ insertion dominates the charge storage process rather than Zn^{2+} insertion or Zn^{2+}/H^+ co insertion. There is also H^+ dependent conversion reaction, in this mechanism the proton causes the chemical conversion of the active material. Finally, the last mechanism to mention is the H^+ dependent dissolution/deposition reaction, this has been reported in MnO_2 cathodes and leads to structural changes in the material. [69]

The presence of two distinct peaks in the curves suggests a potential two-step reaction, where the first step involves the deinsertion of Zn ions, followed by the deinsertion of H^+ ions. However, this conclusion remains hypothetical. Further electrochemical characterization, along with structural and pH analysis of the electrolyte is required to accurately determine the exact mechanism of this process. Perhaps the lack of a second peaks in some of the voltammograms is due to overlapping of Zn^{2+}/H^{+} co-insertion/deinsertion mechanism.

To summarize, electrochemical behavior observed in the voltammograms suggests a complex charge storage mechanism involving Zn^{2+} and H^{+} insertion/deinsertion. The presence of two oxidation and two reduction peaks in certain compositions indicates the coexistence of two distinct charge storage mechanisms, likely corresponding to Zn^{2+} and H^{+} insertion/deinsertion in the electrode material. In contrast, the absence of a second oxidation peak in some cases may result from overlapping Zn^{2+}/H^{+} charge storage mechanisms. However, this conclusion remains hypothetical. Further electrochemical characterization, along with structural and pH analysis of the electrolyte is required to accurately determine the exact mechanism of this process. The reversibility of these redox reactions varies across compositions, with some exhibiting well-defined peaks, indicating stable charge/discharge behavior, while others display broader or less distinct peaks. Furthermore, aluminum doping subtly changes the oxidation and reduction peak's potentials, indicating a modified redox environment. Further electrochemical and structural analysis is necessary to clarify the exact reaction pathways involved.

After completing the CV measurements, SEM analysis was conducted on several anodes and cathodes to examine any structural changes resulting from the electrochemical cycling. Since the electrodes displayed similar morphological features, the ZFOA 5% sample was chosen as a representative example. The following images show both pristine and cycled electrodes for comparison.

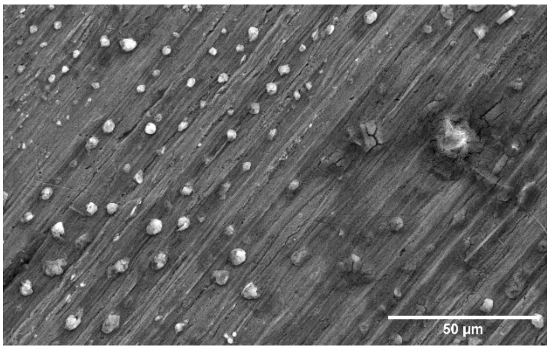

Figure 28 SEM image of zinc metal after 7 CV cycles

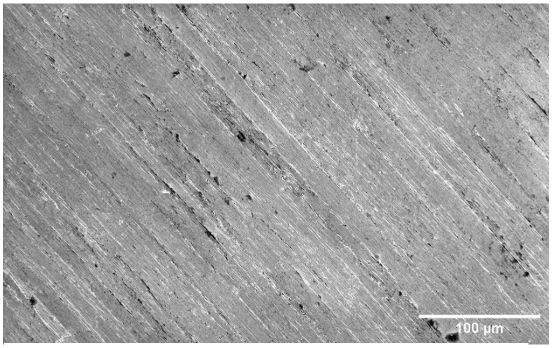

Figure 29 SEM image of pristine zinc metal

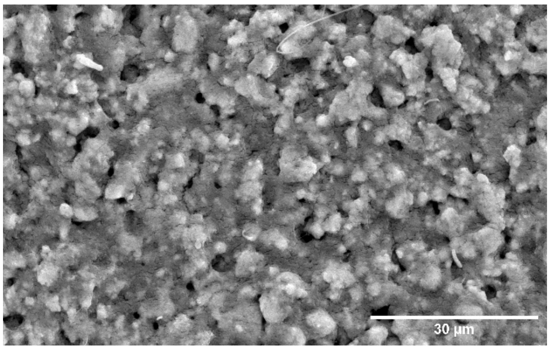

Figure 30 SEM image of ZFOA 5% electrode after 7 CV cycles

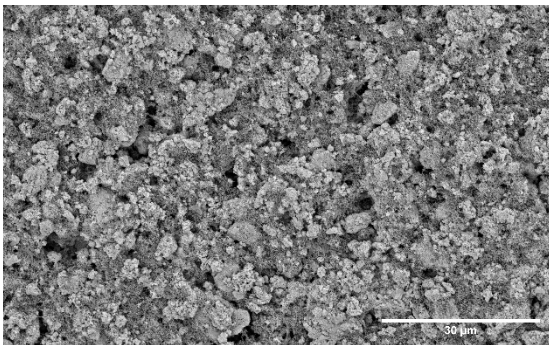

Figure 31 SEM image of pristine ZFOA 5% electrode

As can be seen from the above images, there is formation of crystals on the zinc metal's surface which suggests dendrite formation. This is a common deposition issue caused by the uneven Zn^{2+} stripping/plating reactions on the negative electrode's surface. The reason for this is that the zinc surface is not smooth on an atomic level, which leads to the non-uniform distribution of electrons and ions at the interface, thus causing inhomogeneous nucleation. [70]

The mechanism behind this is that the the H^+ and OH^- made available by the aqueous electrolyte will result in a spontaneous reaction on the surface of the zinc anode. $Zn(OH)_2$ is formed which will then be reduced to ZnO and metallic Zn which are the main culprits of the dendrite formation.[71] This formation might cause short circuits, and might lead to lower the reversibility of the batteries resulting in poor electrochemical performance and shortage of a batteries lifespan. [72]

There is some ongoing research for mitigating this problem, such as modification of electrolytes, [73] the improvement of the structure of the anode[74], as well as coating with protective layers [75].

The positive electrode on the other hand in figure 28 displays a slight formation of salts on the surface, the reason for this phenomenon might be the formation of basic zinc salts. According to literature, the H^+ insertion that is accompanied by the Zn^{2+} insertion in zinc ion batteries raises the local pH, facilitating the formation of basic zinc salts which then buffers pH fluctuations and supports the proton insertion and deinsertion. These precipitated salts are only loosely attached to the cathode surface, making them very prone to detaching in rest periods after discharge. However, during the next charge, proton deinsertion will make the pH at the surface of the electrode very acidic since the pH cannot be buffered anymore. Thus, the proton concentration near the electrode will increase continuously, which will make the proton departure from the active material and thus make the charge and discharge process irreversible. This formation can lead to the loss of salt from the electrolyte, loss of water solvent leading to electrolyte drying and salt crystallization and increase in charge transfer resistance at the electrolyte/electrode interface. [76]

5.8. Galvanostatic Charge and Discharge

Galvanostatic cycling measurements were performed on the most promising materials to evaluate their electrochemical behavior and cyclability potential. The compositions with aluminum content from 0% to 50% showed the following curves:

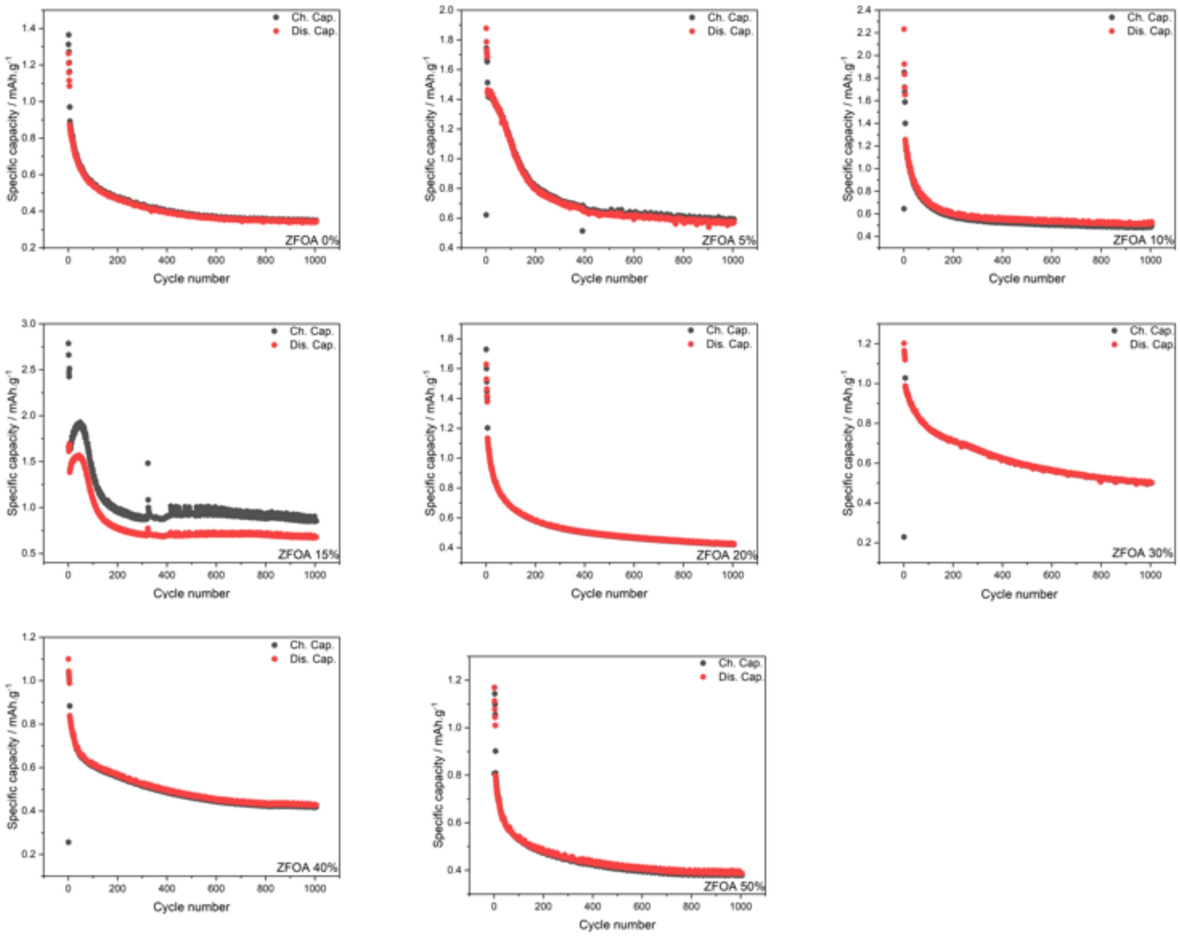

Figure 32 Galvanostatic cycling measurements of ZFOA in the concentration range between 0% and 50% using the positive electrodes as working electrode, zinc metal as counter electrode, 3M zinc triflate as electrolyte and zinc as reference electrode in a voltage range between 0.7 V and 1.8 V with 0.1C

One can see from figure 32, that the pure zinc ferrite shows an initial discharge specific capacity of 1.26 mAh.g^{-1}, after 1000 cycles only 42.06% of the initial capacity is retained. The standout composition ZFOA 10% shows an initial discharge capacity of 2.23 mA·g^{-1} which is still very low, but in comparison to ZFOA 0% is somewhat higher and after 1000 cycles 23.69 % of the discharge capacity is retained.
In the second most promising composition ZFOA 15%, the initial discharge capacity is 1.66 mAh·g^{-1} and after 1000 cycle 40.36 % of the initial capacity is retained.

All the rest of the cells showed very similar behavior. The compounds ZFOA 5% and ZFOA 20% showed a slightly higher initial discharge specific capacity compared to ZFOA 30%, 40% and 50% however they displayed a lower capacity retention (30.48% and 25.92%) at 1000 cycles.

On the other hand, ZFOA 30% and ZFOA 40% showed a higher capacity retention at 1000 cycles, at values of 41.66% and 38.18%. ZFOA 50% showed a poor initial specific discharge capacity at 1.16 mAh.g^{-1} and poor capacity retention of 26.25% at 1000 cycles.

To summarize the results, ZFOA 0% surprisingly showed the best capacity retention after the 1000 cycle, meanwhile the ZFOA 10% had the highest specific discharge capacity but also the lowest capacity retention after 1000 cycles.
Except for ZFOA 5%, there is a clear overlap between the charge and discharge capacities for all tested compounds, indicating a relatively stable Coulombic efficiency after initial cycling. However, a rapid capacity loss is observed during the first few hundred cycles, suggesting instability in the system, possibly due to electrode degradation or loss of active material.

It is important to note that these values may not accurately represent the exact cycling behavior of the compounds. This is due to several factors, including the susceptibility of the anode to corrosion, uneven zinc deposition during cycling, and potential degradation of the electrode interfaces. Additionally, further optimization of the anode, active material, and electrolyte is necessary to enhance overall cell performance and stability. As such, these results primarily serve as a preliminary assessment, providing insights into cycling behavior of the tested materials and their feasibility for future applications.

Similarly, to CV electrodes, the used electrodes in GCD measurements were also examined under SEM after 1000 cycles to identify any morphological changes resulting from prolonged cycling.

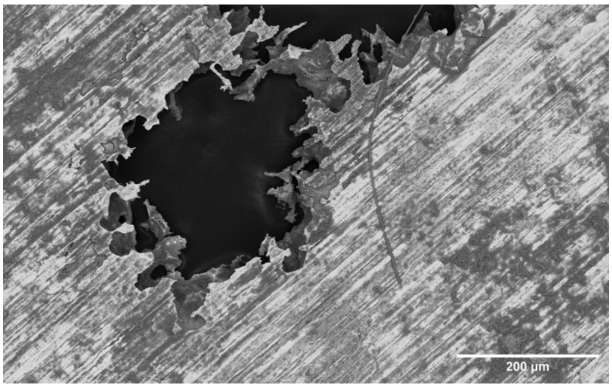

Figure 33 SEM image of zinc metal after 1000 cycles

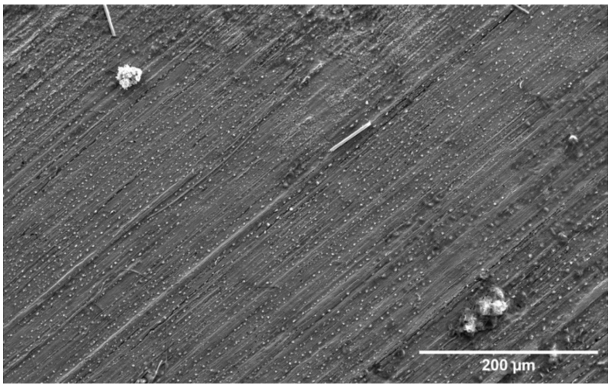

Figure 34 SEM image of zinc metal after 1000 cycles

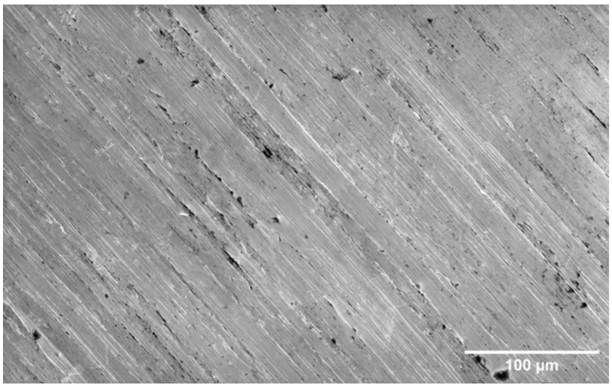

Figure 35 SEM image of pristine zinc metal

As it can be seen from the above pictures when comparing the pristine zinc anode, the cycled anode from the ZFOA 5% cell is corroded with a major dendrite formation. Compared to the electrode pictures after the CV measurements, the state of the electrode is significantly worse due to longer cycling.

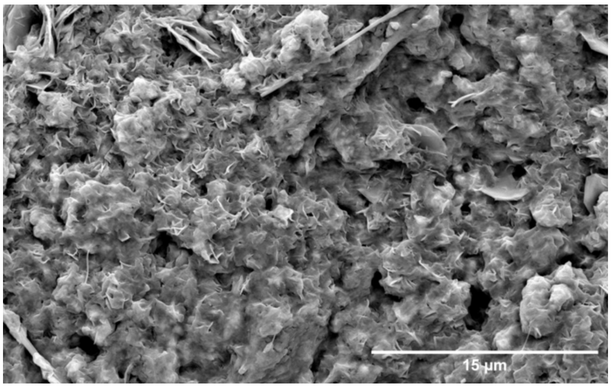

Figure 36 SEM image of ZFOA 15% electrode after 1000 cycles

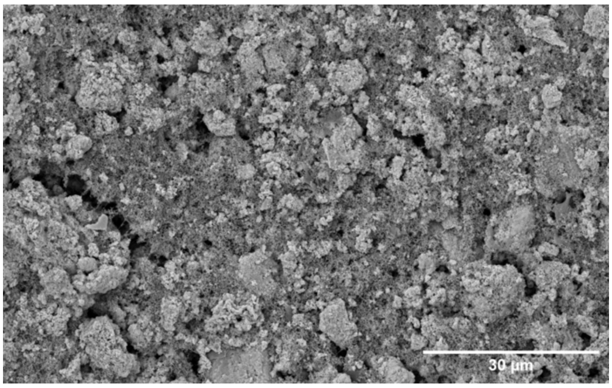

Figure 37 SEM image of pristine ZFOA 15% electrode

Upon comparing the uncycled 15% ZFOA electrode with the one from the cycled ZFOA 15% cell, a noticeable crystal-like structure is observed on the surface of the cycled electrode. This could be indicative of the formation of basic zinc salts, as previously mentioned, which may arise from side reactions during cycling.

These findings further emphasize the need for optimization of the battery components, including the cathode, anode, and electrolyte, to enhance stability and improve cycling behavior.

5.9. KPFM

To measure the surface potential difference between the grain and grain boundaries, KPFM measurements were performed for ZFOA 0%, ZFOA 50% and ZFOA 100%. These measurements will enable the determination of the changes in the potential between grain interior and grain boundary. These changes are associated with accumulation of defects which in turn effects the conductivity. [77]

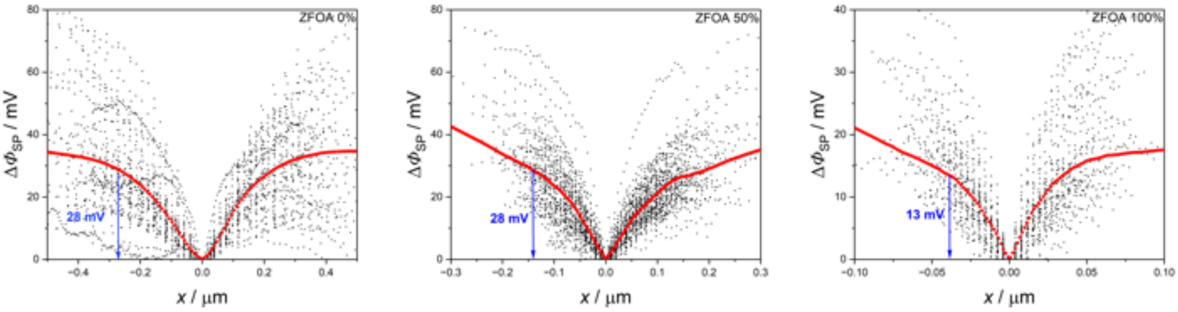

Figure 38 KPFM data of ZFOA 0% (left), ZFOA 50% (middle), ZFOA 100% (right) normalized with respect to the peak position, which is localized in the middle of the grain boundary (bottom). The red line represents the average KPFM data of the raw data shown as black dots. The average KPFM data of the raw data is shown as black dots. The average potential between the grain core and grain boundary is shown by the blue arrow.

The reason for choosing the turning point is because the charge layer of the grain boundary is ending at that point. As observed in the images above, no clear trend can be discerned from the data. Both pure zinc ferrite and the 50% aluminum-doped compound exhibit the same potential difference of 28 mV. In contrast, pure zinc aluminate shows a somewhat lower potential difference of 13 mV. However, this value in zinc aluminate does not necessarily indicate higher conductivity in the material. Rather, it may suggest a reduction in defects around the grain boundaries, which could influence the charge transport pathways. Thus, from the data there is no dependence of the aluminum concentration on the potential barrier around the grain boundaries that can be concluded.

5.10. NIR-Emission Spectra

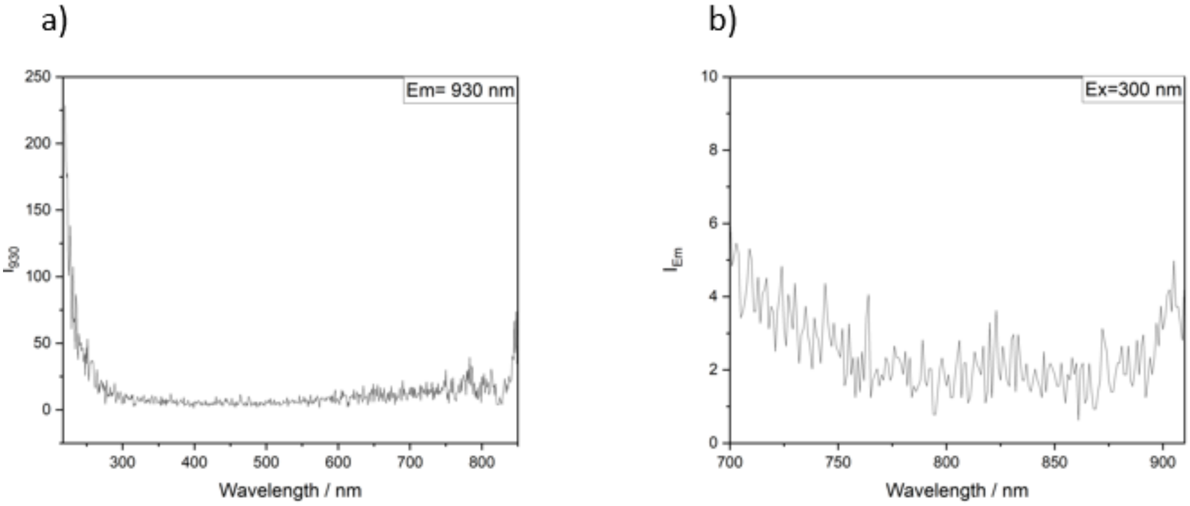

Figure 39 a) excitation spectrum of ZFOA 0% (λ_{em}= 930 nm), b) emission spectrum of ZFOA 0% (λ_{ex}= 300 nm)

As can be seen from the spectra, there are no detectable peaks in the emission and excitation spectra for the pure zinc ferrite. This indicates that pure zinc ferrite does not display any photoluminescence.

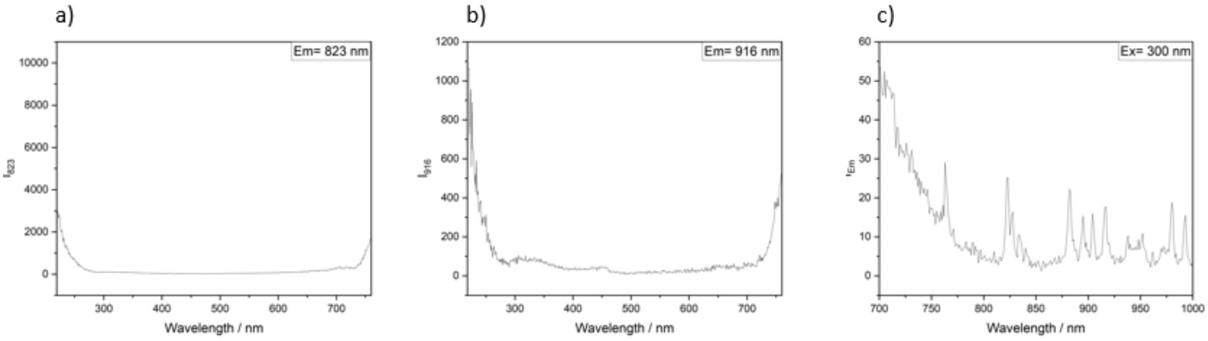

Figure 40 a) excitation spectrum of ZFOA 90% (λ_{em}= 823 nm), b) excitation spectrum of ZFOA 90% (λ_{em}= 916 nm), c) emission spectrum of ZFOA 90% (λ_{ex}= 300 nm)

Since it was expected that the compounds with higher iron content will not results in any response, the second compound to be tested was the compound with 90% aluminum and 10% iron. This also shows no response in the excitation spectra in figure 40, the observed peaks in the emission spectra are merely background noise rather than true luminescence signals. This suggests that the material does not exhibit intrinsic photoluminescence.

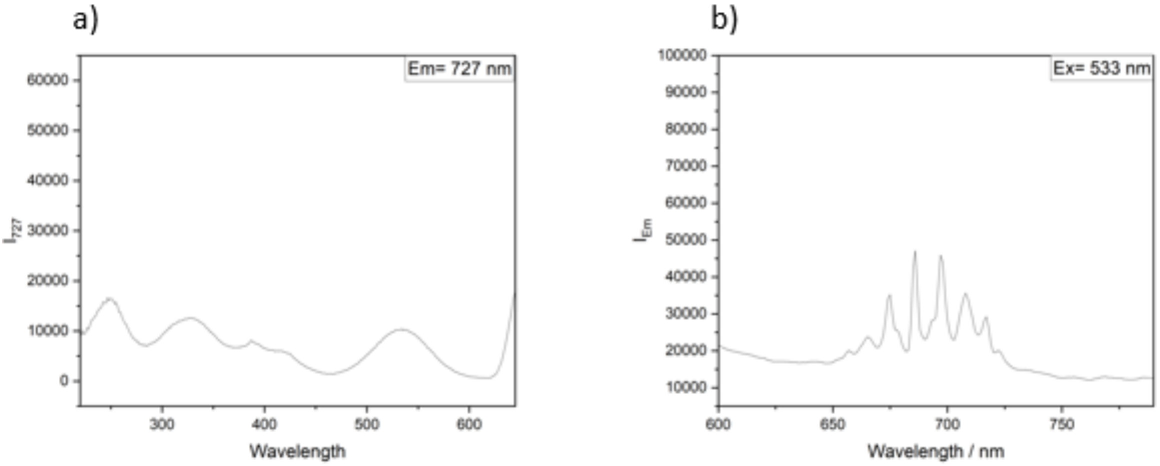

Figure 41 a) excitation spectrum of ZFOA 100% (λ_{em}= 727 nm), b) emission spectrum of ZFOA 100% (λ_{ex}= 533 nm)

Finally, the last material tested was pure zinc aluminate, which exhibited a clear photoluminescence response. A distinct peak was observed in the emission spectrum, attributed to Cr^{3+} impurities present in all aluminate compounds.

In contrast, these Cr^{3+} related peaks were absent in the previously tested iron-containing compounds. This is due to Fe^{3+} being a well-known quencher of photoluminescence, effectively suppressing any emission. The strong quenching effect of Fe^{3+} prevents the detection of Cr^{3+} luminescence in all iron-containing samples. Fe^{3+} is a strong PL quencher because it rapidly diverts excited-state energy into nonradiative channels through energy transfer.

The existence of Cr^{3+} might also explain the difference noticed in the reflectance spectra at higher aluminum concentrations. Perhaps due to the chromium in the metal precursor, this may lead to formation of some new phases.

5.11. Magnetic Susceptibility Determination

To determine the effect of Aluminum doping on the magnetic properties of the zinc ferrites, magnetic susceptibility measurements were conducted.

The data represented bellow shows the effect of aluminum doping on the volume magnetic susceptibility of zinc ferrite. As Al^{3+} increases from 0% to 100% there is a notable decreasing trend in the magnetic properties of the material

Table 7 Magnetic susceptibility at different Al^{3+} contents

Al^{3+} content %	X_v
0	$4.676 \cdot 10^{-4}$
5	$3.842 \cdot 10^{-4}$
10	$3.481 \cdot 10^{-4}$
15	$3.305 \cdot 10^{-4}$
20	$3.048 \cdot 10^{-4}$
30	$3.206 \cdot 10^{-4}$
40	$3.336 \cdot 10^{-4}$
50	$1.992 \cdot 10^{-4}$
60	$1.922 \cdot 10^{-4}$
70	$0.939 \cdot 10^{-4}$
80	$0.539 \cdot 10^{-4}$
90	$0.219 \cdot 10^{-4}$
100	$-0.003 \cdot 10^{-4}$

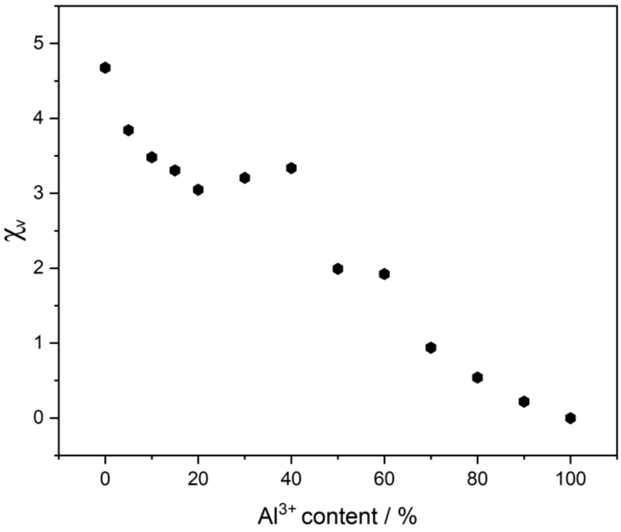

Figure 42 Magnetic susceptibility vs Al^{3+} content

Initially the pure zinc ferrite exhibits a relatively high magnetic susceptibility ($X_v = 4.676 \cdot 10^{-4}$), as the aluminum content increase there a prominent decrease in the values which indicates the significant effect aluminum doping has on the magnetic properties of the material. This is due to the continuous substitution of iron which is a magnetic metal ion with aluminum that is nonmagnetic. There is a slight increase in magnetic susceptibility values for the compounds with 30% and 40% aluminum content, this might have a relation to the degree of inversion in those material.

The lowest value ($X_v = -0.003 \cdot 10^{-4}$) is observed at 100% aluminum content (pure zinc aluminate), the negative value indicates a transition to a diamagnetic behavior, where the material starts to exhibit a reverse response to the magnetic field.

6. Conclusions

As summarization, this study's goal was to produce and investigate the solid solution series $ZnFe_2O_4 - ZnAl_2O_4$. The primary goal was the investigation of these compounds for the application as active material for ZIBs/ZMBs applications. Specifically, the concentration range between 0% and 50% aluminum was investigated for battery application using electrochemical characterization techniques, meanwhile the whole composition was characterized for its structural, optical as well as magnetic properties.

The compounds were made through the Pechini synthesis method, and phase purity was confirmed with the XRD measurements. The compounds yielded a decrease is density as well as decrease in lattice parameter due to the smaller nature of aluminum. Furthermore, a lower grain size was observed with increasing aluminum concentration.

The concentration ranges that yielded the highest conductivity were the compounds with 10% aluminum doping in first place followed by the 15% aluminum content. The rest of the compounds generally displayed a decrease in conductivity with increase of incorporation of aluminum in the structure. An accurate determination of the effect of aluminum on ionic conductivity cannot be made due to the technique used for the measurements. The band gap was determined for all compounds, the pure zinc ferrite displayed a band gap energy of 2.02 eV which agrees with the values taken from literature. The increase in aluminum resulted in a widening of the band gap and thus the change of the compounds from semi conducting to a more insulating state.

The application of the active material in cells for CV and GCD measurements was successful. The voltammograms displayed battery-like behavior and suggested the possibility of a two-step charge storage mechanism, potentially involving both Zn^{2+} and H^+ insertion/deinsertion. A general decrease in cell voltages was observed with increasing aluminum content, which may indicate changes in the electrochemical properties of the material. GCD measurements were successfully performed in three-electrode cells, but the data revealed relatively low discharge specific capacity and poor capacity retention after 1000 cycles.
These findings suggest that while the active material shows potential for reversible Zn^{2+} (and possibly H^+) insertion/deinsertion, further optimization of the battery components is necessary for improved performance in future applications. This need for optimization is highlighted by the observed corrosion and salt formation on the anode and cathode, which significantly impacts the long-term stability and efficiency of the cell.

Overall, all components behaved as expected with the variation in Al-doping. The findings suggest that Al-doped zinc ferrite holds significant potential as an active material for battery applications. The next step should be to optimize all components of the battery system—such as the cathode, anode, electrolyte—to enhance performance, improve cycling stability, and ensure long-term reliability.

7. Sources

[1] W. Ji *et al.*, “Aqueous Zn−organic batteries: Electrochemistry and design strategies,” *Battery Energy*, vol. 2, no. 6, Nov. 2023, doi: 10.1002/bte2.20230020.

[2] A. Konarov, N. Voronina, J. H. Jo, Z. Bakenov, Y.-K. Sun, and S.-T. Myung, “Present and Future Perspective on Electrode Materials for Rechargeable Zinc-Ion Batteries,” *ACS Energy Letters*, vol. 3, no. 10, pp. 2620–2640, Oct. 2018, doi: 10.1021/acsenergylett.8b01552.

[3] M. Song, H. Tan, D. Chao, and H. J. Fan, “Recent Advances in Zn-Ion Batteries,” *Advanced Functional Materials*, vol. 28, no. 41, Oct. 2018, doi: 10.1002/adfm.201802564.

[4] A. A. Kebede, T. Kalogiannis, J. Van Mierlo, and M. Berecibar, “A comprehensive review of stationary energy storage devices for large scale renewable energy sources grid integration,” *Renewable and Sustainable Energy Reviews*, vol. 159, p. 112213, May 2022, doi: 10.1016/j.rser.2022.112213.

[5] G. Fang, J. Zhou, A. Pan, and S. Liang, “Recent Advances in Aqueous Zinc-Ion Batteries,” *ACS Energy Letters*, vol. 3, no. 10, pp. 2480–2501, Oct. 2018, doi: 10.1021/acsenergylett.8b01426.

[6] Y. A. Morkhova, M. Rothenberger, T. Leisegang, S. Adams, V. A. Blatov, and A. A. Kabanov, “Computational Search for Novel Zn-Ion Conductors—A Crystallochemical, Bond Valence, and Density Functional Study,” *The Journal of Physical Chemistry C*, vol. 125, no. 32, pp. 17590–17599, Aug. 2021, doi: 10.1021/acs.jpcc.1c02984.

[7] S. Gbadamasi, S. Loomba, M. W. Khan, B. Shabbir, and N. Mahmood, “Zinc Batteries: Basics, Materials Functions, and Applications,” in *Handbook of Green and Sustainable Nanotechnology*, Springer International Publishing, 2022, pp. 1–37. doi: 10.1007/978-3-030-69023-6_106-1.

[8] P. Lu, Z. Fan, C. Guo, and J. Liang, “Recent Progresses of Aqueous Zinc-Ion Batteries and Their Prospects in the Field of Smart City,” *Advanced Sustainable Systems*, vol. 8, no. 6, Jun. 2024, doi: 10.1002/adsu.202300545.

[9] N. R. Chodankar *et al.*, “Zn-ion Batteries: Charge Storing Mechanism and Development Challenges,” *ChemSusChem*, vol. 16, no. 21, Nov. 2023, doi: 10.1002/cssc.202300730.

[10] P. Kumari and R. Kundu, “Zinc-Ion Batteries: Promise and Challenges for Exploring the Post-Lithium Battery Materials,” *ACS Applied Energy Materials*, vol. 7, no. 21, pp. 9634–9669, Nov. 2024, doi: 10.1021/acsaem.4c02016.

[11] S. Zuo, X. Xu, S. Ji, Z. Wang, Z. Liu, and J. Liu, “Cathodes for Aqueous Zn-Ion Batteries: Materials, Mechanisms, and Kinetics,” *Chemistry – A European Journal*, vol. 27, no. 3, pp. 830–860, Jan. 2021, doi: 10.1002/chem.202002202.

[12] L. E. Blanc, D. Kundu, and L. F. Nazar, “Scientific Challenges for the Implementation of Zn-Ion Batteries,” *Joule*, vol. 4, no. 4, pp. 771–799, Apr. 2020, doi: 10.1016/j.joule.2020.03.002.

[13] J. Ming, J. Guo, C. Xia, W. Wang, and H. N. Alshareef, “Zinc-ion batteries: Materials, mechanisms, and applications,” *Materials Science and Engineering: R: Reports*, vol. 135, pp. 58–84, Jan. 2019, doi: 10.1016/j.mser.2018.10.002.

[14] M. Bohra, V. Alman, and R. Arras, "Nanostructured ZnFe2O4: An Exotic Energy Material," *Nanomaterials*, vol. 11, no. 5, p. 1286, May 2021, doi: 10.3390/nano11051286.

[15] S. Krämer *et al.*, "Teaching an old dog new tricks: Ti-doped ZnFe2O4 as active material in zinc ion batteries – a proof of concept," *Energy Advances*, vol. 3, no. 9, pp. 2175–2185, 2024, doi: 10.1039/D4YA00134F.

[16] L. Rocchetti, A. Amato, and F. Beolchini, "Recovery of indium from liquid crystal displays," *Journal of Cleaner Production*, vol. 116, pp. 299–305, Mar. 2016, doi: 10.1016/j.jclepro.2015.12.080.

[17] V. Tsurkan, H.-A. Krug von Nidda, J. Deisenhofer, P. Lunkenheimer, and A. Loidl, "On the complexity of spinels: Magnetic, electronic, and polar ground states," *Physics Reports*, vol. 926, pp. 1–86, Sep. 2021, doi: 10.1016/j.physrep.2021.04.002.

[18] R. S. Ningthoujam and A. K. Tyagi, Eds., *Handbook of Materials Science, Volume 2*. Singapore: Springer Nature Singapore, 2024. doi: 10.1007/978-981-97-4646-0.

[19] P. Sharma, G. K. Bhargava, S. Bhardwaj, and I. Sharma, Eds., *Engineered Ferrites and Their Applications*. Singapore: Springer Nature Singapore, 2023. doi: 10.1007/978-981-99-2583-4.

[20] R. B. Jordan, *Principles of Inorganic Chemistry*. Cham: Springer International Publishing, 2024. doi: 10.1007/978-3-031-22926-8.

[21] M. A. Raza *et al.*, "Synthesis and characterization of zinc aluminate electrodes for supercapacitor applications," *Electrochimica Acta*, vol. 475, p. 143501, Jan. 2024, doi: 10.1016/j.electacta.2023.143501.

[22] A. R. West, *Solid State Chemistry and Its Applications.* 2nd ed. Chichester, West Sussex: John Wiley & Sons, Ltd, 2014.

[23] B. Guillaume, "Etude des mécanismes de conduction électrique dans des matériaux composites pour application d'anode inerte. Relation conductivité-composition/microstructure", Ecole Nationale Supérieure des Mines de Saint-Etienne, Saint-Étienne, 2008.

[24] J. Öijerholm, "Ionic Transport in Metal Oxides Studied in situ by Impedance Spectroscopy and Cyclic Voltammetry," Royal Institue of technology, Stockholm, 2007.

[25] Z. W. B. Iton and K. A. See, "Multivalent Ion Conduction in Inorganic Solids," Feb. 08, 2022, *American Chemical Society*. doi: 10.1021/acs.chemmater.1c04178.

[26] P. J. Gellings, *The CRC Handbook of SOLID STATE Electrochemistry*. CRC Press, 2019. doi: 10.1201/9780429121791.

[27] J. E. House, "Defects in solids," in *Introduction to Solid State Chemistry*, Elsevier, 2024, pp. 35–54. doi: 10.1016/B978-0-443-13426-5.00010-4.

[28] M. Reynaud, J. Serrano-Sevillano, and M. Casas-Cabanas, "Imperfect Battery Materials: A Closer Look at the Role of Defects in Electrochemical Performance," *Chemistry of Materials*, vol. 35, no. 9, pp. 3345–3363, May 2023, doi: 10.1021/acs.chemmater.2c03481.

[29] R. J. D. Tilley, *Principles and Applications of Chemical Defects*. Routledge, 2019. doi: 10.1201/9780203742228.

[30] A. E. Danks, S. R. Hall, and Z. Schnepp, "The evolution of 'sol–gel' chemistry as a technique for materials synthesis," *Materials Horizons*, vol. 3, no. 2, pp. 91–112, 2016, doi: 10.1039/C5MH00260E.

[31] T. O. L. Sunde, T. Grande, and M.-A. Einarsrud, "Modified Pechini Synthesis of Oxide Powders and Thin Films," in *Handbook of Sol-Gel Science and*

Technology, Cham: Springer International Publishing, 2016, pp. 1–30. doi: 10.1007/978-3-319-19454-7_130-1.

[32] L. Dimesso, “Pechini Processes: An Alternate Approach of the Sol–Gel Method, Preparation, Properties, and Applications,” in *Handbook of Sol-Gel Science and Technology*, Cham: Springer International Publishing, 2016, pp. 1–22. doi: 10.1007/978-3-319-19454-7_123-1.

[33] Y. Waseda, E. Matsubara, and K. Shinoda, *X-Ray Diffraction Crystallography*. Berlin, Heidelberg: Springer Berlin Heidelberg, 2011. doi: 10.1007/978-3-642-16635-8.

[34] J. Kawai, *X-Ray Spectroscopy for Chemical State Analysis*. Singapore: Springer Nature Singapore, 2023. doi: 10.1007/978-981-19-7361-1.

[35] Raymond A. Serway and Jr. John W. Jewett, *Physics for Scientists and Engineers with Modern Physics*, 7th ed. Belmont: Thomson Learning, Inc, 2008.

[36] A. B. Spierings, M. Schneider, and R. Eggenberger, “Comparison of density measurement techniques for additive manufactured metallic parts,” *Rapid Prototyping Journal*, vol. 17, no. 5, pp. 380–386, Aug. 2011, doi: 10.1108/13552541111156504.

[37] C. J. William D and David G. Rethwisch, *Materials Science and Engineering,* 10th ed. Danvers: John Wiley & Sons, Inc., 2018.

[38] A. Ul-Hamid, *A Beginners’ Guide to Scanning Electron Microscopy*. Cham: Springer International Publishing, 2018. doi: 10.1007/978-3-319-98482-7.

[39] L. Reimer, *Scanning Electron Microscopy*, vol. 45. Berlin, Heidelberg: Springer Berlin Heidelberg, 1998. doi: 10.1007/978-3-540-38967-5.

[40] Evgenij Barsoukov and J. Ross Macdonald, Eds., *Impedance Spectroscopy Theory, Experiment, and Applications*, 2nd ed. Hoboken: John Wiley & Sons, Inc., 2005.

[41] Ramanathan Srinivasan and Fathima Fasmin, *An Introduction to Electrochemical Impedance Spectroscopy*, 1st ed. Danvers: CRC Press, 2021.

[42] A. Ch. Lazanas and M. I. Prodromidis, “Electrochemical Impedance Spectroscopy─A Tutorial,” *ACS Measurement Science Au*, vol. 3, no. 3, pp. 162–193, Jun. 2023, doi: 10.1021/acsmeasuresciau.2c00070.

[43] A. Lasia, *Electrochemical Impedance Spectroscopy and its Applications*. New York, NY: Springer New York, 2014. doi: 10.1007/978-1-4614-8933-7.

[44] J. T. S. Irvine, D. C. Sinclair, and A. R. West, “Electroceramics: Characterization by Impedance Spectroscopy,” *Advanced Materials*, vol. 2, no. 3, pp. 132–138, Mar. 1990, doi: 10.1002/adma.19900020304.

[45] J. A. N. T. Soares, “Introduction to Optical Characterization of Materials,” in *Practical Materials Characterization*, New York, NY: Springer New York, 2014, pp. 43–92. doi: 10.1007/978-1-4614-9281-8_2.

[46] T. Jüstel and S. Schwung, *Leuchtstoffe, Lichtquellen, Laser, Lumineszenz*. Berlin, Heidelberg: Springer Berlin Heidelberg, 2019. doi: 10.1007/978-3-662-55950-5.

[47] R. López and R. Gómez, “Band-gap energy estimation from diffuse reflectance measurements on sol–gel and commercial TiO2: a comparative study,” *Journal of Sol-gel Science and Technology*, vol. 61, no. 1, pp. 1–7, Jan. 2012, doi: 10.1007/s10971-011-2582-9.

[48] H. Yamada, K. Yoshii, M. Asahi, M. Chiku, and Y. Kitazumi, “Cyclic Voltammetry Part 1: Fundamentals,” *Electrochemistry*, vol. 90, no. 10, pp. 22–66082, Oct. 2022, doi: 10.5796/electrochemistry.22-66082.

[49] N. Elgrishi, K. J. Rountree, B. D. McCarthy, E. S. Rountree, T. T. Eisenhart, and J. L. Dempsey, “A Practical Beginner’s Guide to Cyclic Voltammetry,”

Journal of Chemical Educcation, vol. 95, no. 2, pp. 197–206, Feb. 2018, doi: 10.1021/acs.jchemed.7b00361.

[50] X. Yang and A. L. Rogach, “Electrochemical Techniques in Battery Research: A Tutorial for Nonelectrochemists,” *Advanced Energy Materials*, vol. 9, no. 25, Jul. 2019, doi: 10.1002/aenm.201900747.

[51] T. Schoetz, L. W. Gordon, S. Ivanov, A. Bund, D. Mandler, and R. J. Messinger, “Disentangling faradaic, pseudocapacitive, and capacitive charge storage: A tutorial for the characterization of batteries, supercapacitors, and hybrid systems,” *Electrochimica Acta*, vol. 412, p. 140072, Apr. 2022, doi: 10.1016/j.electacta.2022.140072.

[52] Seizo Morita, Ed., *Roadmap of scanning probe microscopy.* Berlin: Springer-Verlag, 2007.

[53] F. Xia, I. W. Rangelow, and K. Youcef-Toumi, *Active Probe Atomic Force Microscopy*. Cham: Springer International Publishing, 2024. doi: 10.1007/978-3-031-44233-9.

[54] S. Sadewasser and T. Glatzel, Eds., *Kelvin Probe Force Microscopy*, vol. 65. Cham: Springer International Publishing, 2018. doi: 10.1007/978-3-319-75687-5.

[55] Bernard Valeur, *Molecular Fluorescence: Principles and Applications*. Weinheim: Wiley-VCH Verlag GmbH, 2001.

[56] Douglas A. Skoog, F. James Holler, and Stanley R. Crouch, *Principles of Instrumental Analysis*, 7th ed. Boston: Cengage Learning, 2016.

[57] S. Mugiraneza and A. M. Hallas, “Tutorial: a beginner’s guide to interpreting magnetic susceptibility data with the Curie-Weiss law,” *Communications Physics*, vol. 5, no. 1, p. 95, Apr. 2022, doi: 10.1038/s42005-022-00853-y.

[58] R. L. Carlin, *Magnetochemistry*. Berlin, Heidelberg: Springer Berlin Heidelberg, 1986. doi: 10.1007/978-3-642-70733-9.

[59] D. F. Evans, “A new type of magnetic balance,” *Journal of Physics E*, vol. 7, no. 4, pp. 247–249, Apr. 1974, doi: 10.1088/0022-3735/7/4/007.

[60] Howard E. Swanson, Howard F. McMurdie, Marlene C. Morris, Eloise H. Evans, and Boris Paretzkin, “Standard X-ray Diffraction Powder Patterns,” vol. Section 9, no. Data for 63 Substances.

[61] H. M. Widatallah *et al.*, “On the synthesis and cation distribution of aluminum-substituted spinel-related lithium ferrite,” *Materials Letters*, vol. 59, no. 8–9, pp. 1105–1109, Apr. 2005, doi: 10.1016/j.matlet.2004.12.017.

[62] D. W. Richerson and W. E. Lee, *Modern Ceramic Engineering*. CRC Press, 2018. doi: 10.1201/9780429488245.

[63] C. B. Carter and M. G. Norton, *Ceramic Materials*. New York, NY: Springer New York, 2013. doi: 10.1007/978-1-4614-3523-5.

[64] R. Pandit, K. K. Sharma, P. Kaur, R. K. Kotnala, J. Shah, and R. Kumar, “Effect of Al3+ substitution on structural, cation distribution, electrical and magnetic properties of CoFe2O4,” *Journal of Physics and Chemistry of Solids*, vol. 75, no. 4, pp. 558–569, Apr. 2014, doi: 10.1016/j.jpcs.2013.12.015.

[65] S. A. Saafan, A. S. Seoud, and R. E. El Shater, “Theoretical investigation of some experimental data of Al-substituted MnZn spinel ferrites,” *Physica B: Condensed Matter*, vol. 365, no. 1–4, pp. 27–42, Aug. 2005, doi: 10.1016/j.physb.2005.04.034.

[66] Z.-X. Zhu *et al.*, “Deciphering H+/Zn2+ co-intercalation mechanism of MOF-derived 2D MnO/C cathode for long cycle life aqueous zinc-ion batteries,” *Rare Metals*, vol. 41, no. 11, pp. 3729–3739, Nov. 2022, doi: 10.1007/s12598-022-02088-w.

[67] W. Sun *et al.*, “Zn/MnO2 Battery Chemistry With H+ and Zn2+ Coinsertion,” *Journal of the American Chemical Society*, vol. 139, no. 29, pp. 9775–9778, Jul. 2017, doi: 10.1021/jacs.7b04471.

[68] K. Zhu, T. Wu, S. Sun, W. van den Bergh, M. Stefik, and K. Huang, “Synergistic H+/Zn2+ dual ion insertion mechanism in high-capacity and ultra-stable hydrated VO2 cathode for aqueous Zn-ion batteries,” *Energy Storage Materials*, vol. 29, pp. 60–70, Aug. 2020, doi: 10.1016/j.ensm.2020.03.030.

[69] W. Li *et al.*, “Proton Storage Chemistry in Aqueous Zinc-Inorganic Batteries with Moderate Electrolytes,” *Advanced Materials*, vol. 37, no. 10, Mar. 2025, doi: 10.1002/adma.202414019.

[70] J. Yan *et al.*, “High-Voltage Zinc-Ion Batteries: Design Strategies and Challenges,” *Advanced Functional Materials*, vol. 31, no. 22, May 2021, doi: 10.1002/adfm.202010213.

[71] H. J. Kim, S. Kim, K. Heo, J. Lim, H. Yashiro, and S. Myung, “Nature of Zinc-Derived Dendrite and Its Suppression in Mildly Acidic Aqueous Zinc-Ion Battery,” *Advanced Energy Materials*, vol. 13, no. 2, Jan. 2023, doi: 10.1002/aenm.202203189.

[72] V. Ho, H. Lim, M. J. Kim, and J. Mun, “Improving the Performance of Aqueous Zinc-ion Batteries by Inhibiting Zinc Dendrite Growth: Recent Progress,” *Chemistry: An Asian Journal*, vol. 17, no. 14, Jul. 2022, doi: 10.1002/asia.202200289.

[73] H. Tian *et al.*, “Steel Anti-Corrosion Strategy Enables Long-Cycle Zn Anode,” *Advanced Energy Materials*, vol. 13, no. 1, Jan. 2023, doi: 10.1002/aenm.202202603.

[74] Q. Cao *et al.*, “Gradient design of imprinted anode for stable Zn-ion batteries,” *Nature Communications*, vol. 14, no. 1, p. 641, Feb. 2023, doi: 10.1038/s41467-023-36386-3.

[75] L. Kang *et al.*, “Nanoporous CaCO3 Coatings Enabled Uniform Zn Stripping/Plating for Long-Life Zinc Rechargeable Aqueous Batteries,” *Advanced Energy Materials*, vol. 8, no. 25, Sep. 2018, doi: 10.1002/aenm.201801090.

[76] V. Verma, S. Kumar, W. Manalastas, and M. Srinivasan, “Undesired Reactions in Aqueous Rechargeable Zinc Ion Batteries,” *ACS Energy Letters*, vol. 6, no. 5, pp. 1773–1785, May 2021, doi: 10.1021/acsenergylett.1c00393.

[77] K. Neuhaus and H.-D. Wiemhöfer, “Electrochemical characteristics of grain boundaries in gadolinium and aluminum co-doped ceria and ceria-alumina composites,” *Solid State Ionics*, vol. 371, p. 115771, Nov. 2021, doi: 10.1016/j.ssi.2021.115771.

8. List of figures

9. List of tables